

High precision spectro-temporal analysis of ultra-fast radio bursts using per-channel arrival times

Mohammed A. Chamma,^{1,2*} Victor Pop² and Fereshteh Rajabi²

¹*Department of Physics and Astronomy, The University of Western Ontario, 1151 Richmond Street, London, Ontario N6A 3K7, Canada*

²*Department of Physics and Astronomy, McMaster University, Hamilton, Ontario L8S 4L8, Canada*

Accepted XXX. Received YYY; in original form ZZZ

ABSTRACT

Fast radio bursts (FRBs), especially those from repeating sources, exhibit a rich variety of morphologies in their dynamic spectra (or waterfalls). Characterizing these morphologies and spectro-temporal properties is a key strategy in investigating the underlying unknown emission mechanism of FRBs. This type of analysis has been typically accomplished using two-dimensional Gaussian techniques and the autocorrelation function (ACF) of the waterfall. These techniques suffer from high uncertainties when applied to recently observed ultra-FRBs: FRBs that are only a few microseconds long. We present a technique that involves the tagging of per-channel arrival times of an FRB to perform sub-burst slope measurements. This technique leverages the number of frequency channels and can increase the precision of sub-burst slope measurements by several orders of magnitude, allowing it to be easily applied to ultra-FRBs and microshot forests. While scattering and dispersion remain important and often dominating sources of uncertainty in measurements, this technique provides an adaptable and firm foundation for obtaining spectro-temporal properties from all kinds of FRB morphologies. We present measurements using this technique of several hundred bursts across 12 repeating sources, including over 400 bursts from the repeating sources FRB 20121102A, FRB 20220912A, and FRB 20200120E, all of which exhibit microsecond-long FRBs, as well as 136 drift rates. In addition to retrieving the known relationship between sub-burst slope and duration, we explore other correlations between burst properties. We find that ultra-FRBs obey the sub-burst slope law along with longer duration bursts, and appear to form a distinct population in the duration-frequency relation.

Key words: radiation: dynamics – relativistic processes – radiation mechanisms: non-thermal

1 INTRODUCTION

Fast radio bursts (FRBs) exhibit a diverse and rich set of information through their spectro-temporal properties, often yielding clues to the underlying physical processes of these extremely distant, energetic, and short-lived (~ 1 ms) coherent bursts.

FRBs are broadly categorized into repeating and non-repeating sources, which exhibit different statistical properties in their burst bandwidths and durations (Pleunis et al. 2021b; Petroff et al. 2022). This observation precludes the possibility that some non-repeating sources have simply not yet been observed to repeat.

Repeating sources offer opportunities for continued monitoring and source localization, and often emit bursts with complex time-frequency structure not displayed by non-repeating sources. Examples of this structure include the presence of multiple sub-components within a single burst event, as well as the observed tendency for later components to drift to lower frequencies (the “sad-trombone effect”; Hessels et al. 2019). This effect has been analogously observed within a single burst, where lower frequency components arrive slightly delayed relative to higher frequencies, referred to as the sub-burst slope law and/or intra-burst drift rate (Rajabi et al. 2020; Chamma et al. 2021, 2023; Jahns et al. 2023; Brown et al. 2024). This effect is observed even after the frequency

dependent ($\propto \nu^{-2}$) delaying influence due to interstellar dispersion is removed, although the dispersion measure (DM) used can greatly affect measurements when characterizing drift rates and sub-burst slopes.

Spectro-temporal properties, such as the duration, bandwidth, frequency, energy, drift rate and sub-burst slope, reveal interesting and unexpected relationships between one another that serve as constraints on physical emission or source models. For example, Hewitt et al. (2022) observed two distinct groups of bursts in the width-bandwidth-energy parameter space for bursts from repeater FRB 20121102A (Spitler et al. 2016; Scholz et al. 2016; Marcote et al. 2017; Bassa et al. 2017; Chatterjee et al. 2017; Tendulkar et al. 2017). Multiple studies have now observed a bimodal distribution in burst wait times (Li et al. 2021; Hewitt et al. 2022; Jahns et al. 2023), as well as in burst energies (Li et al. 2021) for FRB 20121102A.

A particularly strong correlation, which is a primary focus of this study, has been observed between the sub-burst duration and sub-burst slope/intra-burst drift in bursts from multiple repeating sources. First seen strongly in bursts from FRB 20121102A (Rajabi et al. 2020; Chamma et al. 2023; Jahns et al. 2023), it appears that multiple other repeating sources exhibit the same relationship and even share the same scaling (Chamma et al. 2021; Wang et al. 2022; Brown et al. 2024). This correlation is predicted by the triggered relativistic dynamical model (TRDM) whereby the FRB source, moving at up-to relativistic velocities relative to an observer, is triggered by an

* E-mail: mchamma@uwo.ca

incident energy source (such as emission from a magnetar) located behind it and along the line of sight (Rajabi et al. 2020). In other words, the relationship can be interpreted as the direct result of dynamical (relativistic) motions in the FRB source that modulate the signal through the Doppler effect and differing reference frames between the source and the observer. This relationship takes the form of $dt/d\nu \propto \sigma_t$ where $dt/d\nu$ is the inverse sub-burst slope, or the change in burst arrival time with frequency, and σ_t is the sub-burst duration. In earlier works (Rajabi et al. 2020; Chamma et al. 2021, 2023), $d\nu/dt$ was used as the sub-burst slope, however, this leads to a singularity for bursts with little to no drift in time. Therefore, we adopt the recommendation of Jahns et al. (2023) to formulate the measurement as the inverse instead. Hereafter we will interchangeably refer to $dt/d\nu$ as the sub-burst slope or intra-burst drift.

As the number of bursts and the number of repeaters analysed grows, the robustness of the sub-burst slope relation ($dt/d\nu \propto \sigma_t$) is increasingly demonstrated. In the course of such analyses, there is growing evidence from the results of Chamma et al. (2023), Jahns et al. (2023), and Brown et al. (2024) that an analogous and/or identical relation exists for the drift rates of multiple components of an FRB and their overall duration. The interpretation of this is not clear but suggests a connection between the physical process that gives rise to drift within sub-bursts and the process that causes drift among distinct burst components.

Recently, multiple studies have reported the discovery of ultra FRBs—FRBs of microsecond or even nanosecond durations—in bursts from FRB 20121102A (Snelders et al. 2023) and FRB 20200120E (Nimmo et al. 2022, 2023; Pearlman et al. 2023). Additionally, bursts featuring dense forests of microshots have been observed from FRB 20220912A, a recently discovered and highly active repeater (Hewitt et al. 2023; Zhang et al. 2023; Sheikh et al. 2024a). Understanding where the spectro-temporal properties of these ultra-FRBs fall is a valuable test of known spectro-temporal relationships and extends the measured parameter space by several orders of magnitude. Deviations (or the lack thereof) that may be observed are also significant, as these three sources are localized to disparate environments. For example, FRB 20200120E is localized to a globular cluster (Kirsten et al. 2022), while FRB 20220912A lacks a persistent radio source (Hewitt et al. 2024) seen in other repeating sources such as FRB 20121102A.

Gaussian formalisms have been used thus far in the literature to perform spectro-temporal analyses of bursts, including measurements of drift rate and sub-burst slope (e.g. Hessels et al. 2019; Rajabi et al. 2020; Chamma et al. 2021, 2023; Jahns et al. 2023; Brown et al. 2024). In Hessels et al. (2019), a two-dimensional (2D) Gaussian model is fitted to the 2D autocorrelation function (ACF) of the burst waterfall, and burst properties are calculated from the model parameters. Jahns et al. (2023) introduced several 2D Gaussian models that could be fitted directly to the waterfall of an FRB and used parameters with physically consistent dimensionality; i.e., the burst properties are parameters of the Gaussian model, and the fits directly yield a measurement. As we shall discuss, all the Gaussian methods presented in the literature thus far appear to exhibit a large covariance between the sub-burst slope and duration, meaning that relative uncertainties in sub-burst slope measurements approach infinity as burst duration decreases. This issue can prevent the analysis of ultra-FRBs using Gaussian methods due to the unconstrained uncertainties. Other modelling techniques that produce accurate spectral models of FRBs exist, such as `burstfit` (Aggarwal et al. 2021) and `fitburst` (Fonseca et al. 2023); however, these do not lend themselves easily to acquiring sub-burst slope measurements due to their underlying formalism. Additional work must therefore be done to

accurately calculate the uncertainties when using Gaussian methods, or an entirely different technique should be used to obtain accurate measurements when analysing the properties of ultra-FRBs.

This work will present a technique that relies on tagging the arrival time of an FRB signal in each frequency channel of its waterfall, which yields precise sub-burst slope measurements when applied to ultra-FRBs. Using the arrival time data, one can apply various models to characterize the drifting behaviour of a burst. We apply a simple linear model to define the sub-burst slope measurement. This method is detailed in Section 2. We apply this method to obtain measurements for hundreds of FRBs from 12 different repeating FRB sources, with a strong focus on the three aforementioned repeaters that have exhibited ultra-FRBs or microshot behaviour: FRB 20121102A, FRB 20220912A, and FRB 20200120E. The data used are described and summarized in Section 3. Section 4 details the results of these measurements, including figures showing the sub-burst slope relation and other correlations, as well as presenting drift rate measurements from bursts with multiple components. Section 4 also includes a comparison between the arrival times and Gaussian methods to demonstrate the prohibitively large relative uncertainties obtained when using Gaussian methods on ultra-FRBs and to highlight the circumstances that give rise to differing measurements.

Finally, in Section 5, we discuss the interpretation of our results, possible extensions of the arrival times method, and directions for future analyses. The paper is summarized in Section 6. An abridged table of burst measurements can be found in Appendix A, sorted by shortest duration and Appendix B provides an example measurement of a microshot forest.

2 METHODOLOGY

2.1 Arrival times pipeline

Gaussian methods for obtaining the sub-burst slope, whether by fitting to the 2D autocorrelation of an FRB or to the FRB waterfall directly often suffer from low precision when bursts are short-duration, near vertical, or low-S/N. By using the arrival time of an FRB in each frequency channel of its waterfall, we can improve the precision of sub-burst slope (i.e., intra-burst drift) measurements, especially for ultra-FRBs (microsecond long FRBs). Filtering for arrival times in channels with sufficiently high S/N (we chose 3σ) helps with measurement accuracy and quality.

The outline of the procedure is as follows:

- (i) Given a waterfall, first compute the 1D time series integrated over all frequency channels.
- (ii) Fit a 1D Gaussian to the time series. If multiple components (sub-bursts) are present in the waterfall, model the time series as the sum of multiple 1D Gaussians. The width, σ_t , of this 1D Gaussian is used as the duration measurement of the burst (or sub-burst component if there are multiple components).
- (iii) For each component of the 1D time series, use a multiple of its width (we chose $4\sigma_t$) to select a time range on either side and cut out the burst component from its waterfall.
- (iv) For each frequency channel (row) of the waterfall, fit a 1D Gaussian to model the pulse in that frequency channel. The 1D Gaussian model used throughout (including for the time series fit) is given by:

$$G(t) = A \exp\left(-\frac{(t-t_0)^2}{2\sigma^2}\right), \quad (1)$$

with parameters A , t_0 , and σ . The “arrival time” of the FRB in that

frequency channel is then defined as

$$t_{\text{arr}} \equiv t_0 - \sqrt{2}\sigma, \quad (2)$$

which corresponds to the e^{-1} amplitude of the Gaussian. This point in time is found for each frequency channel.

(v) Apply spectral and temporal filters to arrival time data: we find the S/N of the pulse in each frequency channel using the mean of pixels in the on-pulse region and the standard deviation of any pixels in an off-pulse region in the same channel, while ensuring that the noise is sampled over the same number of pixels used to measure the signal. If the S/N is greater than 3σ in that channel, the arrival time in that channel is considered acceptable and retained for use in subsequent steps. The on-pulse region for each component is determined using the position $t_{0,1D}$ and width $\sigma_{t,1D}$ from the 1D Gaussian fit obtained from the integrated time series. This is generally sufficient for ensuring that arrival times accurately correspond to their burst in the waterfall. Nonetheless, an additional filter is applied to remove arrival times at durations greater than $2\sigma_{t,1D}$ away from the component time from the integrated time series fit.

(vi) Using the arrival times that remain after applying the filters, a linear fit of the form

$$t_{\text{arr}} = \frac{dt}{d\nu} \nu + t_b \quad (3)$$

is performed. This defines the inverse sub-burst slope $dt/d\nu$ ¹ and is how the measurement is obtained. The intercept value t_b is a constant offset necessary for a general linear model to accurately converge and does not have a physical meaning associated with the FRB. Technically, t_b represents the ‘arrival time’ relative to the peak of the pulse if the burst extended to a frequency of 0, which, of course, is not observed. To further illustrate this, the parameter t_b can be removed if ν is replaced with $\nu - \nu_{\text{offset}}$, where ν_{offset} is a different offset parameter, now in units of frequency, that is also purely numerical. Both choices result in the same measured value of $dt/d\nu$.

(vii) The burst duration σ_t and bandwidth σ_ν of each burst are obtained from the 1D Gaussian fits of the integrated time-series and spectrum of each component, respectively. The center frequency ν_0 of the FRB is defined as the peak of the fit to the integrated spectrum. In some cases, intensity variations due to scintillation can interfere with the measurement, resulting in an underestimated value for the burst bandwidth. For example, a burst may have a high intensity over only a small fraction of its total bandwidth. In such cases, some channels are masked based on a manually determined intensity threshold and ignored during fitting, which helps yield a broader, more accurate bandwidth.

An additional step is performed in the presence of multiple components to measure the drift rate between components. Using the center frequency ν_0 and the time of each component, obtained from the integrated 1D spectrum and time series, a line analogous to that in Equation 3 is fitted to define the drift rate $\Delta t/\Delta\nu$. We measure the ‘total duration’ of an FRB with multiple components, which may have unpredictable spacings between them, as the time difference between the first and last components. This estimate of the duration turns out to be sufficient for our purposes, though other definitions may be required depending on the research goals.

Figure 1 illustrates the method applied to both an FRB with a single component and an FRB with multiple components, including

a drift rate measurement. Appendix A provides an abridged table of measurements sorted by shortest duration.

There are many instances of bursts with components that overlap or blend together. In such cases, we can still obtain reasonably good measurements by manually selecting where to cut out the bursts, rather than using the $4\sigma_t$ width used in step (iii). By using multiple manual cuts, we can separate many components and obtain measurements. This strategy can even be applied to microshot forests (e.g., Hewitt et al. 2023), where one burst has over 40 components, with significant success. However, this process is still limited by the amount of blending in the waterfall and the ability to visually distinguish components. Figure 2 shows an example of measurements from a blended two-component burst. Appendix B provides additional details on the process and challenges of analysing heavily blended microshot waterfalls using the arrival times method.

The arrival times method provides several advantages. Namely, since the measurement of $dt/d\nu$ is obtained using a number of data points on the order of the number of frequency channels (in high S/N cases), the precision of the sub-burst slope can be up to a few orders of magnitude higher than in earlier methods (Section 4.3), which used 2D Gaussian fits to the autocorrelation or directly to the burst waterfall (see e.g. Chamma et al. 2021, 2023; Jahns et al. 2023). This is especially true for very short bursts.

Additionally, the method naturally allows for different models of the relationship between t_{arr} and frequency to be investigated. This is particularly relevant in light of the complex burst morphologies observed by Faber et al. (2023), who argue for power law models to describe the drifting morphologies they observe.

The arrival times pipeline is implemented in Python and packaged with FRBGUI² (though currently only in script form) and is also accessible via the Zenodo link provided at the end of the paper. Technical documentation is also available³.

Note that this method, along with the other methods mentioned here, does not consider the covariance of the measurements with the dispersion measure (DM) or with scattering effects. Typically, a strategy must be applied before performing measurements to account for these significant and often dominant sources of uncertainty. In the case of the DM, this has typically been done by either: (a) performing measurements at each burst’s independently obtained DM, as is done in a majority of the literature; (b) repeating measurements over broad ranges of possible DM values, effectively trading precision for accuracy (e.g., Chamma et al. 2021, 2023; Brown et al. 2024); or (c) assuming the validity of the predicted relationship between t_{arr} and ν (i.e., the sub-burst slope law of Rajabi et al. 2020) to correct the DM such that the deviation from this relationship is minimal (see Jahns et al. 2023 for a quantitative application of this, and Chamma et al. 2023; Brown et al. 2024 for a qualitative application). We will explore here another strategy: using the highly precise DMs of the newly discovered ultra-FRBs to select and impose the DM on the remaining bursts in a sample. We will find that, while this is effective in retrieving expected spectro-temporal relationships, it does not provide any significant advantages over other methods, and may be sensitive to the effects of interstellar scattering. Other possible strategies could involve using the distribution of DMs from a source to better quantitatively estimate the covariance with spectro-temporal properties.

¹ This is identical to the measurement of $(d\nu_{\text{obs}}/dt_D)^{-1}$ and d_t from the formalisms of Rajabi et al. (2020) and Jahns et al. (2023), respectively.

² <https://github.com/mef51/frbgui>

³ <https://frbgui.readthedocs.io/arrivaltimes>

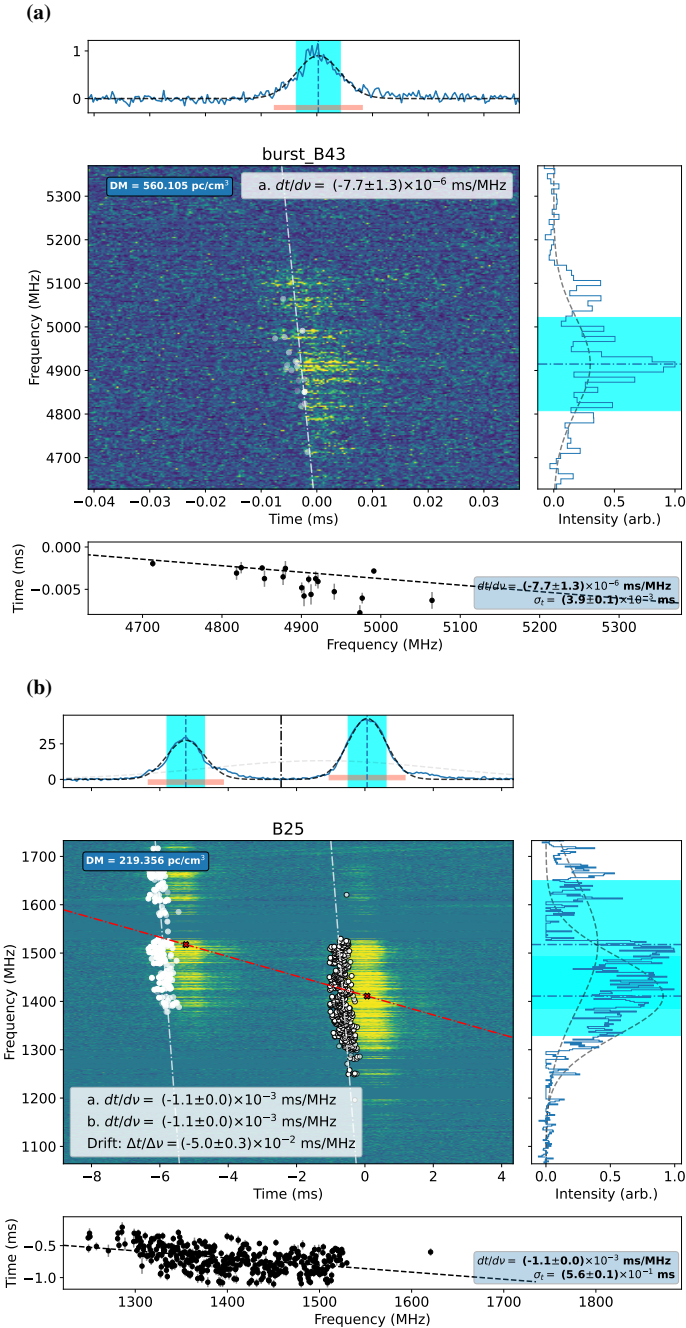


Figure 1. (a) Arrival times method for burst B43 of [Snelders et al. \(2023\)](#).

The top and rightmost panels show the integrated time series and spectrum, respectively, of the waterfall, shown in the center. In the time series, the 1D Gaussian fits are overlaid with a black line. The vertical dashed line denotes the peak time of the burst. The reddish bar indicates the $2\sigma_{t,1D}$ window used in the arrival times temporal filter. The faint blue shaded regions in the time series and spectrum are the 1σ regions of their corresponding fits. The spectrum is found by integrating only over the $1\sigma_{t,1D}$ region of the pulse. The dash-dot line denotes the center frequency. The waterfall is displayed with white points indicating the arrival times of each frequency channel, which are then used in the linear fit to obtain $dt/d\nu$, shown in the bottom sub-panel.

(b) Same as above but for burst B25 of [Sheikh et al. \(2024a,b\)](#), which has two sub-bursts. The plot shows how different components are separated for measurement. Components are labeled alphabetically from left to right and each set of arrival time points are colored according to the sub-burst they are associated with. The red line indicates the drift rate measurement $\Delta t/\Delta\nu$ obtained for this burst and the red xs denote the center frequency of each

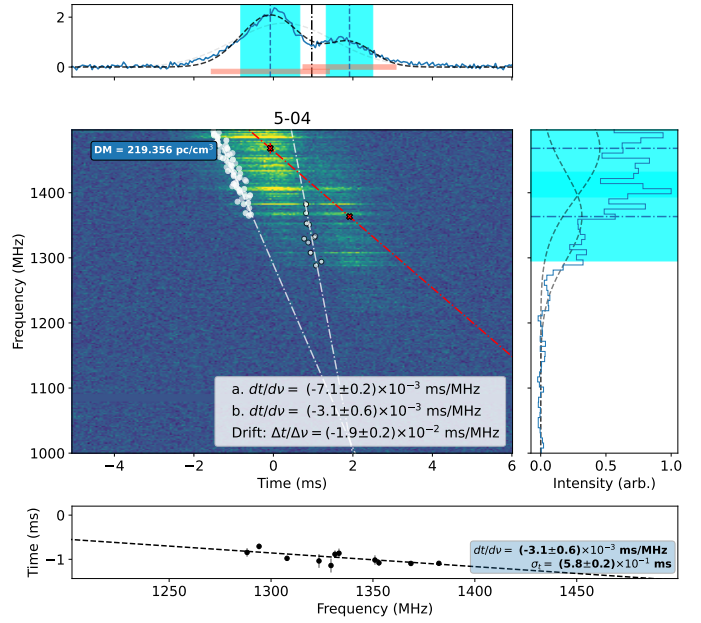


Figure 2. Burst 5-04 from [Zhang et al. \(2023\)](#) from FRB 20220912A. Same as Figure 1, but showcasing measurements from two sub-components blended together. The black dash-dot line in the time series indicates the position of the manual cut.

2.2 Measurement filtering

In order to accurately quantify the relationships between the spectro-temporal measurements obtained from the arrival times pipeline, we apply additional filters to the resulting measurements to exclude those with large uncertainties or invalid values. These typically include measurements from faint, blended, RFI-affected, or otherwise obscured burst pulses.

The primary filters applied remove measurements of bursts with relative uncertainties on their duration or sub-burst slope larger than 100%. While these measurements can still be physically meaningful (e.g., a measurement of a burst with a slope of 2×10^{-4} ms/MHz with $\sim 100\%$ relative uncertainty can still be useful for its order of magnitude), they are not very helpful for exploring or quantifying spectro-temporal relationships between burst properties and can be a hindrance. A subsequent filter removes measurements obtained with only 2 or fewer acceptable arrival times. A more conservative threshold, such as 10 or even 20 or more acceptable arrival times, could be imposed, but this had little effect on our conclusions other than excluding many measurements.

For the datasets analysed here, 1320 measurements were obtained from the arrival times pipeline, and 503 measurements remain after filtering, i.e., about 62% of measurements were excluded. This comes after several rounds of review and efforts to obtain accurate measurements for each pulse in the dataset. The large number of dropped measurements in this sample is primarily due to a significant number of very low S/N bursts that subsequently fail the spectral filter applied when determining valid arrival times.

3 OBSERVATIONS AND DATA

The data used for this study was obtained from previously published observational studies. The majority of the bursts analysed here have

not had measurements of their sub-burst slopes performed before, and we also reanalyse the spectro-temporal properties of many bursts from earlier studies. To the best of our knowledge, the ultra-FRBs analysed here represent the first sub-burst slope measurements for these extremely short bursts. This section provides a brief summary of the repeating FRBs included in this study, with a particular focus on those exhibiting ultra-FRBs or bursts with microsecond-long durations (specifically, FRB 20121102A, FRB 20220912A, and FRB 20200120E). Additionally, we outline the properties of the bursts analysed and describe the DM strategy employed during the measurements. As in earlier studies (Chamma et al. 2023; Brown et al. 2024), we process and convert all data from various formats (e.g., PSRCHIVE, PSRFITS, filterbank, etc.) into Python `numpy` (.npz) format for analysis. The details of this conversion are described here, with reference to previous works where appropriate.

Each burst analysed may have unique inputs to the arrival times pipeline, including the times of sub-bursts, cut placements, mask locations, downsampling factors, and other user-defined options. A measurement script is provided, which lists the options used for each analysed burst and performs the measurements via the arrival times pipeline.

Table 1 lists the 12 repeating FRB sources analysed in this study. For each source, the table provides the corresponding journal reference for the observational study, the telescope facility used, the observational band covered, and the number of sub-bursts obtained. Additionally, the burst duration range covered by the entire cohort of bursts from a source is included.

Figure 3 displays histograms of the burst properties analysed in this study.

3.1 FRB Sources

3.1.1 FRB 20121102A

FRB 20121102A, the first discovered and one of the most well-observed sources of repeating FRBs, exhibits bursts across a broad range of frequencies, a candidate 161 day periodicity in its activity cycle, and has been localized to a bright star-forming region on the outskirts of a dwarf galaxy (Spitler et al. 2016; Scholz et al. 2016; Marcote et al. 2017; Bassa et al. 2017; Chatterjee et al. 2017; Tendulkar et al. 2017; Cruces et al. 2020).

Snelders et al. (2023) reported the discovery of 8 FRBs from FRB 20121102A with microsecond durations, identified through a reanalysis of 2017 data taken with the Green Bank Telescope (GBT). These bursts are orders of magnitude shorter than other known FRBs. The data and processing scripts were made available via a Zenodo link and were adapted to produce .npz files for the arrival times pipeline.

In Chamma et al. (2023), we analysed a subset of the bursts observed by Michilli et al. (2018); Gajjar et al. (2018); Oostrum et al. (2020); Aggarwal et al. (2021) and Li et al. (2021). Waterfalls from these sources were obtained in ASCII, PSRFITS, or filterbank format, and underwent downsampling, dedispersion, and other processing steps before spectro-temporal analysis. A detailed description of how the waterfall data were prepared and converted to Python .npz files can be found in Section 3 of Chamma et al. (2023). These same files were used in re-analysing the data with the arrival times pipeline for this study. We note that burst 11M from Gajjar et al. (2018) potentially consists of two microshots (noticeable at a DM of 560.105 pc/cm^3) that were previously missed. However, these microshots had too low of a S/N to be reliably measured.

Data from Hewitt et al. (2022) included 478 bursts observed dur-

ing a burst storm in 2016. In Brown et al. (2024), 24 of these bursts were analysed using FRBGUI (Chamma et al. 2023). We re-analysed the entire dataset and obtained measurements for 46 sub-bursts, representing a small portion of the total number of bursts (as listed in Table 1). There are several reasons why measurements could not be obtained from the majority of the bursts. These are typically due to very low S/N, high uncertainties arising from the quality of the waterfall data and measurements, as well as radio frequency interference (RFI) in the waterfall.

The final dataset for this source included the six bursts observed by Scholz et al. (2016), which were already provided in .npz format. These are the only bursts in the 2 GHz range for FRB 20121102A that the authors are aware of.

For this dataset we investigated applying the DM of one of the shortest bursts from the source (in this case 560.105 pc/cm^3 from the ultra-FRB B30 of Snelders et al. 2023) to the majority of the data. This approach was chosen because the DM of the shortest burst is likely to have high precision due to its sharp profile. Jahns et al. (2023) also recommend this step when analysing bursts emitted within weeks of each other, as their results suggest that short-term DM variations are caused by intra-burst drift. The data from Hewitt et al. (2022) were not included in this step, and these data were analysed with their applied DM of 560.5 pc/cm^3 . We hypothesized that the DM of the shortest burst could be a highly precise measurement of a source’s DM, which would be indicated by an improved agreement with fits to the sub-burst slope law. However, we observed only slight improvements compared to using each burst’s individual DM. A more thorough investigation into optimizing the DM would also need to account for the source’s DM evolution over time, which we decided to be beyond the scope of this paper. The results of these DM investigations are discussed further in Appendix C.

3.1.2 FRB 20220912A

FRB 20220912A is a recently discovered and highly active repeating source, capable of emitting hundreds of bursts per hour during periods of activity (Zhang et al. 2023). Some of these bursts are exceptionally bright and display dense microshot structures, as observed by Hewitt et al. (2023). The source has been localized to a galaxy with a low host contribution to the DM along the line of sight (Ravi et al. 2023).

The data analysed from Hewitt et al. (2023) were prepared using the scripts provided in that paper’s reproduction package⁴. Since some microshots in this dataset contained over 40 components with varying degrees of blending, we initially used CHIME’s `fitburst` package (Fonseca et al. 2023) to construct a spectral model of the burst with the appropriate number of components, and then extracted the model components for measurement using the arrival times pipeline. Although we were eventually able to produce a reasonably accurate model with the correct number of components, the extracted components appeared too synthetic, and the drifting information within sub-bursts was lost, as the model components were perfectly vertical. Consequently, we reverted to using the feature within the arrival times pipeline that allows for manual selection of each component’s location, along with manually placing cuts between components to mitigate the effects of blending.

We obtained 35 burst waterfalls from Sheikh et al. (2024a) as `numpy` .npz files and PSRFITS archives, however, the .npz files were sufficient and we used those directly. These bursts were observed by

⁴ <https://zenodo.org/records/10552561>

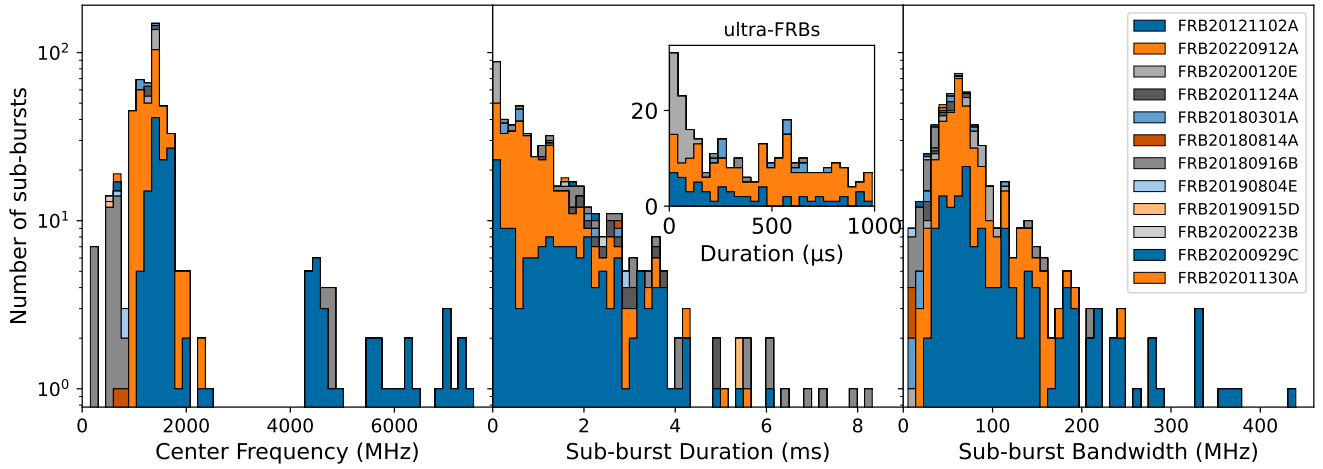


Figure 3. Distribution of burst properties analysed, as measured by the arrival times pipeline. From left to right, the center frequency, sub-burst duration, and sub-burst bandwidth distributions are shown. Bins from each source are stacked. Inset in the middle panel is an additional plot showing the duration distribution of FRBs shorter than 1 ms with a bin width of 40 μ s. Sub-bursts here refers to the components of each FRB, each of which have been separated and measured independently.

FRB Source	Reference	Telescope	Obs. Band (MHz)	Duration Range	Sub-bursts Measured	DM _{applied} (pc/cm ³)
FRB 20121102A	Hewitt et al. 2022	Arecibo	1150 – 1730	1.4 μ s – 6 ms	46	560.5
	Aggarwal et al. 2021	Arecibo	974 – 1774		15	560.105
	Gajjar et al. 2018	GBT	4000 – 8000		14	''
	Michilli et al. 2018	Arecibo	4100 – 4900		14	''
	Oostrum et al. 2020	WSRT	1250 – 1450		13	''
	Li et al. 2021	FAST	1000 – 1500		36	''
	Scholz et al. 2016	GBT	1600 – 2400		4	''
		Arecibo	1150 – 1730		1	''
	Snelders et al. 2023	GBT	3900 – 9300		6	''
FRB 20220912A	Sheikh et al. 2024a	ATA	900 – 2334	9 μ s – 5.5 ms	151	219.356 (see text)
	Hewitt et al. 2023	NRT	1230 – 1742		30	''
	Zhang et al. 2023	FAST	1000 – 1500		56	''
FRB 20200120E	Nimmo et al. 2023	Effelsberg	1200 – 1600	13.1 – 133 μ s	34	87.7527
	Nimmo et al. 2022	Effelsberg	1200 – 1600		4	87.75
FRB 20180916B	CHIME/FRB 2019	CHIME	400 – 800	0.18 – 8.3 ms	15	Burst DM
	Pleunis et al. 2021a	LOFAR	110 – 188		7	348.772
	Marthi et al. 2020	uGMRT	550 – 750		15	348.82
FRB 20201124A	Hilmarsson et al. 2021	Effelsberg	1200 – 1520	1 – 4.9 ms	16	411.60
FRB 20180301A	Luo et al. 2020	FAST	1000 – 1500	0.21 – 2.8 ms	16	Burst DM (~516)
FRB 20180814A	CHIME/FRB et al. 2021	CHIME	400 – 800	1.25 – 2.8 ms	2	Burst DM (~189)
FRB 20200929C	CHIME/FRB et al. 2023	CHIME	''	1.75 – 2.3 ms	2	Burst DM (~413)
FRB 20190804E	''	CHIME	''	0.89 – 7.4 ms	2	Burst DM (~363)
FRB 20190915D	''	CHIME	''	5.3 ms	1	Burst DM (~489)
FRB 20200223B	''	CHIME	''	2.3 ms	1	Burst DM (~202)
FRB 20201130A	''	CHIME	''	1.58 – 4.3 ms	2	Burst DM (~288)
Total: 503						

Table 1. Summary of observations used, including the source, telescope, observational band, duration range, the number of of sub-bursts measured, and the applied DM. As discussed in the text, the DM of a microburst from its respective source is applied to the data for FRB 20121102A (except for the data from Hewitt et al. 2022) and FRB 20220912A. In the remaining datasets the DM applied is either the burst DM on a burst-by-burst basis or the DM applied by the authors of the dataset. For datasets that use the burst DM, the approximate DM for that source is listed in parentheses. The duration range is found using measurements from the arrival times pipeline and covers only the bursts with valid measurements from a source.

the Allen Telescope Array (ATA), which covered a frequency band of 900 – 2334 MHz across multiple tuning configurations. Our analysis also includes over 60 additional FRBs, many with complicated series of components, that were discovered only after publication (Sheikh et al. 2024b). Almost all these additional FRBs exhibited multiple components and ended up forming the majority of measurements obtained from this dataset.

Burst waterfalls from figures 5 and 9 Zhang et al. (2023) were obtained as raw Python arrays at a DM of 220 pc/cm³, and we added metadata such as the frequency axis and DM for use in analysis. Although that study detected 1076 bursts, only those published in the figures were available at the time of analysis. Additionally, we optionally centered and normalized each channel in each waterfall by the off-pulse mean and standard deviation, as this improved the visual clarity of the burst.

Similar to FRB 20121102A, we applied the DM of the microshot forest B1, as determined by Hewitt et al. (2023) (219.356 pc/cm³), to most bursts from this source. The resulting spectro-temporal relationships showed little difference compared to applying individual burst DMs. For the two additional, less complex microshot forests (B2 and B3) from Hewitt et al. (2023), we chose to retain their original DMs of 219.375 and 219.8 pc/cm³, respectively, due to the effort involved in determining those DMs.

3.1.3 FRB 20200120E

FRB 20200120E is a repeating FRB source, currently the closest discovered to our galaxy. Unlike other sources typically found in younger star-forming regions, it is localised to a globular cluster (e.g. Bhardwaj et al. 2021; Kirsten et al. 2022; Nimmo et al. 2023). Its burst morphology is also exceptional, exhibiting structure down to the nano-second scale (Nimmo et al. 2022).

We accessed the five bursts reported in Nimmo et al. (2022) via the Zenodo link provided, which included archive files of the bursts generated from filterbank data. Using `pypulse`, we loaded the archives, dedispersed them to the reported DM of 87.75 pc/cm³ and downsampled the frequency channels by a factor of 8.

For the approximately 60 bursts reported in Nimmo et al. (2023), the data were also available in filterbank format again through a Zenodo link. We used the `your` package to load the data and incoherently dedispersed all bursts to the reported DM of 87.7527 pc/cm³. The data were cropped and normalized by channel to improve burst visibility. Also to boost visibility and S/N, we downsampled the bursts in frequency by a factor of 8 and in time by a factor of 2, except for three bursts detected with a pulsar backend, which had a longer time resolution and were only downsampled in frequency. Additionally, masking was applied to channels affected by RFI across all waterfalls.

3.1.4 Remaining sources

The remaining data were collected from repeating FRB sources as part of the analysis conducted by Brown et al. (2024). We summarize relevant information regarding these sources here and refer the reader to Section 2.2 of Brown et al. (2024) and Table 1 for more details.

FRB 20180916B is a repeating source with a periodic activity cycle of approximately 16 days, exhibiting chromatic activity over the course of its cycle. It is located in a spiral galaxy 149 MPC away (e.g. CHIME/FRB 2020; Tendulkar et al. 2021; Pastor-Marazuella et al. 2021). Data for this source extend to the lowest frequencies observed from FRBs, including the 110 MHz detections reported by Pleunis et al. (2021a).

FRB Source	Fit $\nu \cdot dt/d\nu = a\sigma_t + b$		# Bursts
	a (unitless)	b (ms)	
FRB 20121102A	$(-8.9 \pm 0.1) \times 10^0$	$(1.5 \pm 0.1) \times 10^{-2}$	149
FRB 20220912A	$(-7.10 \pm 0.02) \times 10^0$	$(1.3 \pm 0.0) \times 10^{-1}$	237
FRB 20200120E	$(-1.7 \pm 0.5) \times 10^0$	$(1.1 \pm 1.4) \times 10^{-2}$	38
FRB 20180916B	$(-7.2 \pm 0.3) \times 10^0$	$(3.3 \pm 0.1) \times 10^0$	37
FRB 20201124A	$(-1.8 \pm 0.1) \times 10^1$	$(2.0 \pm 0.2) \times 10^1$	16
FRB 20180301A	$(-1.1 \pm 0.1) \times 10^1$	$(4.7 \pm 0.5) \times 10^0$	16
Total:			493

Table 2. Results of linear fits to sub-burst slope law for each source with more than a few measured bursts. The fit follows the form $\nu(dt/d\nu) = a\sigma_t + b$, where $dt/d\nu$ is the inverse sub-burst slope and σ_t is the sub-burst duration.

Repeaters FRB 20180301A and FRB 20201124A are well-observed sources, with studies frequently focusing on the polarization properties of their emission. Here, we re-analyse bursts from these sources as presented in Luo et al. (2020) and Hilmarsson et al. (2021), respectively.

Data for sources FRB 20180814A, FRB 20190804E, FRB 20190915D, FRB 20200223B, FRB 20200929C, and FRB 20201130A are accessed from the CHIME/FRB burst catalogs (CHIME/FRB 2019; CHIME/FRB et al. 2021; CHIME/FRB et al. 2023).

4 RESULTS

Our analysis provides spectro-temporal measurements for each burst examined, including the center frequency (ν_0), duration (σ_t), bandwidth (σ_ν), and sub-burst slope/intra-burst drift ($dt/d\nu$), along with their uncertainties.

In this section, we explore the correlations between each of the parameters measured in order to verify those observed in Chamma et al. (2023) and Brown et al. (2024) (among others) and to leverage the expanded parameter space afforded by our measurements from ultra-FRBs. We focus on the relation between the (inverse) sub-burst-slope and duration in Figure 4 and present fits to this relationship for each repeating FRB source in Table 2. Additional correlations are shown in Figure 5, with points colored by duration to highlight the parameter space occupied by ultra-FRBs. We will also contextualize the observed spectro-temporal correlations in light of previous findings.

Section 4.2 summarizes the drift rate measurements obtained and their relationship with duration. Section 4.3 presents the results of comparison tests between the arrival times and Gaussian methods, highlighting areas of agreement, conditions under which inconsistencies may arise, and the robust performance of the arrival times method across all duration scales.

4.1 Spectro-temporal relationships

4.1.1 Sub-burst slope vs. duration relation

The sub-burst slope relationship for the measured FRBs is shown in Figure 4, which displays the inverse normalized sub-burst slope $\nu(dt/d\nu)$ versus sub-burst duration. The inset panel highlights measurements from ultra-FRBs, defined here as bursts with durations below an arbitrarily chosen cutoff of 300 μ s. Data points are colored by frequency. In this plot, bursts with a near vertical orientation have a value of $dt/d\nu$ approaching zero. The ultra-FRBs exhibit a strong

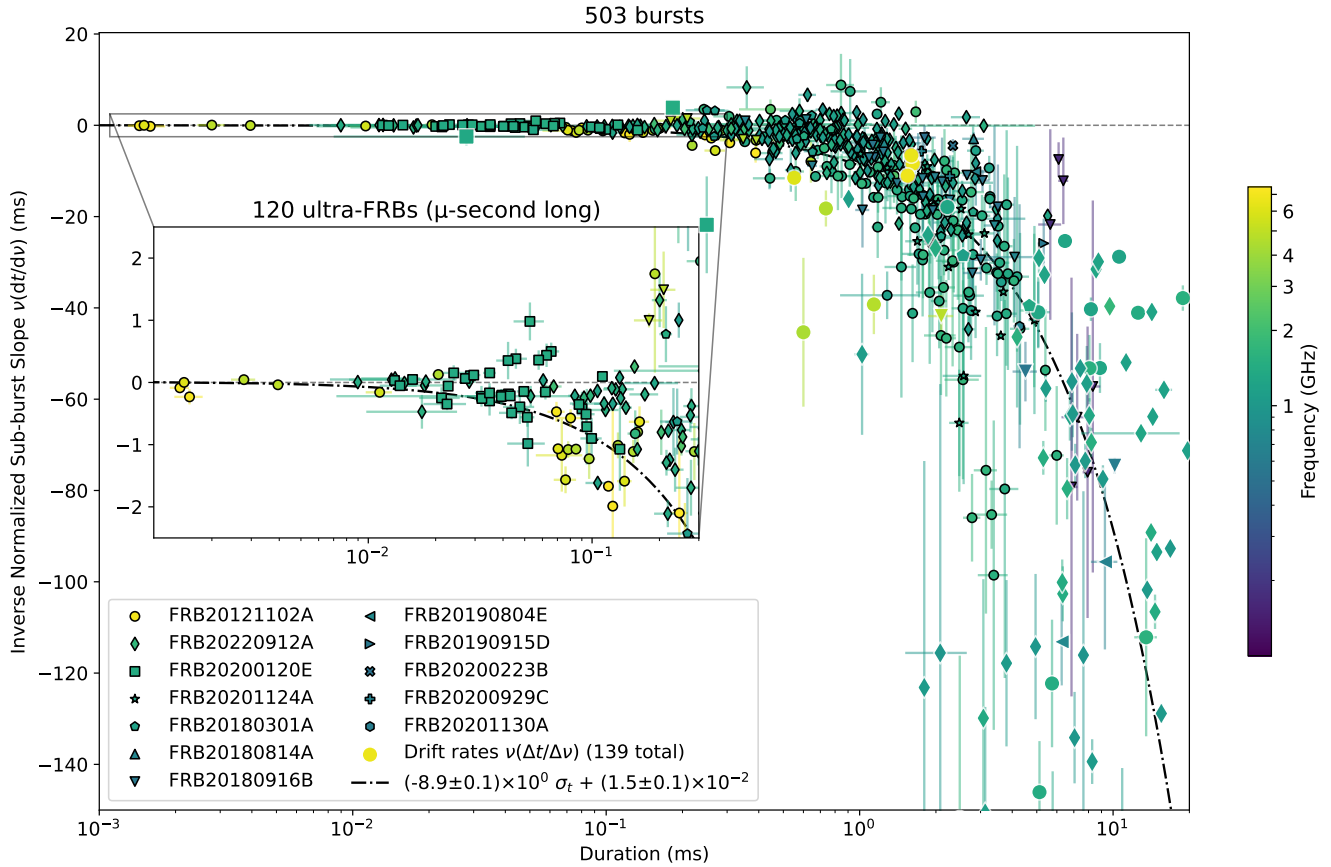


Figure 4. Plot of the inverse normalized sub-burst slope, $v(dt/dv)$, versus the sub-burst duration, σ_τ , for a cohort of FRBs from multiple repeating sources. All measurements were obtained using the arrival times pipeline. The duration axis is displayed on a logarithmic scale. The inset panel provides a zoomed view of ultra-FRBs with durations below our selected upper limit of 300 μ s. The marker shape denotes the source of the burst, while bursts are colored by frequency, ranging from around 100 MHz to nearly 7.5 GHz. The dashed line represents a general linear fit to the data from FRB 20121102A, the source with the most extensive set of observations. See the text for details on the DMS used for measurements. Overall, we observe good agreement with the linear fit across all sources within the uncertainties, consistent with previous analyses. Drift rate measurements obtained from waterfalls with multiple components are overlaid with slightly larger markers and a white border. These measurements generally align with the fit for sub-burst slopes, but they exhibit more outliers. Some drift rates fall outside the chosen axis limits.

clustering around zero, with fluctuations diminishing as the duration decreases.

The predicted relationship between sub-burst slope and duration for FRBs is provided in Equation 7 of [Rajabi et al. \(2020\)](#). In the formalism used here, this relationship is inverted, taking the following linear form

$$v \frac{dt}{dv} = -A\sigma_\tau, \quad (4)$$

where A is a constant. To evaluate the agreement with this predicted relationship, we fit the data using the general linear form $v(dt/dv) = a\sigma_\tau + b$, applying orthogonal distance regression ([Boggs & Rogers 1990](#)) via the `scipy.odr` package. This method incorporates uncertainties in both the dependent and independent variables when determining the best fit.

Table 2 presents the results of these fits for each FRB source analysed. The fit for FRB 20121102A, which includes 149 bursts measured and covers the widest range of frequencies and durations, yields $a = -8.9 \pm 0.1$ and $b = (0.015 \pm 0.001)$ ms. This fit is shown as the black dash-dot line in Figure 4. Note that the curved appearance of the fit line results from the logarithmic scale used on the duration

axis. Due to the general form of the fit, agreement with Equation 4 is in practice captured by the magnitude of b , where a value near zero indicates good agreement and larger values suggest otherwise. Assuming that b must be zero (i.e., that the sub-burst relation holds true) allows b to serve as an indicator of data quality. A large b may result from a limited variety or incomplete sample of bursts in terms of frequency and/or duration. This trend is evident in Table 2 for the remaining sources, where a fluctuates around the value found for FRB 20121102A, while b generally increases significantly as the number of available bursts decreases. An exception to this is FRB 20200120E, possibly due to a sampling bias toward very short bursts. FRB 20220912A also tests this rule since b is large despite the large number of bursts. This may be due to an actual deviation from the sub-burst slope law for this source.

We can compare our result of $a = -8.9 \pm 0.1$ for FRB 20121102A with previous analyses. In [Brown et al. \(2024\)](#), using measurements from 65 sub-bursts, a value of $A = 0.076 \pm 0.004$ was obtained for FRB 20121102A using the inverse form of Equation 4. Converting to our formalism gives $a_1 = 1/A = 13.2 \pm 0.7$. Similarly, [Chamma et al. \(2023\)](#) found $A = -0.113 \pm 0.003$ for FRB 20121102A using

167 bursts. Converting that value gives $a_2 = -8.9 \pm 0.2$, identical to the result found here within uncertainties. In [Jahns et al. \(2023\)](#), approximately half of the 849 bursts observed from FRB 20121102A in the 1150 – 1730 MHz band were analysed for intra-burst drift using a 2D Gaussian fit that directly included the drift as a parameter d_t . This measurement of d_t has the same dimensions as $dt/d\nu$ used here, describing the same property of a burst, and can therefore be directly compared (App. A of [Jahns et al. 2023](#)). When performing a linear fit of the form $d_t = b\sigma_t + c$, [Jahns et al. \(2023\)](#) found $b = -0.00862 \text{ MHz}^{-1}$ and $c = 0.00171 \text{ ms/MHz}$. Converting to the present formalism requires multiplying by their mean burst frequency of $\sim 1450 \text{ MHz}$, yielding $a_3 = -12.5$. The three fit values for the sub-burst slope relation of FRB 20121102A from earlier studies- a_1, a_2, a_3 -are therefore quite close, with a_2 matching the value of a obtained here, despite the significant methodological differences. For example, [Chamma et al. \(2023\)](#) and [Brown et al. \(2024\)](#) fit a 2D Gaussian to the ACF of the burst waterfall, while [Jahns et al. \(2023\)](#) used a differently parametrized 2D Gaussian fit directly to the burst waterfall. Slight differences in the resulting fit values can be due to the smaller number of bursts used, as in the cases of a_1 and a_2 , or from the limited frequency range in the case of a_3 , as well as the absence of measurements from ultra-FRBs until now. Other differences may stem from variations in the definition of sub-burst duration. Despite these factors, we observe close agreement between the earlier fit values of the sub-burst slope relation for FRB 20121102A and the value obtained here.

4.1.2 Relations between ν_0 , σ_t , σ_ν and $dt/d\nu$

Additional correlations between the spectro-temporal properties of the analysed FRBs are presented in the corner plot in Figure 5. The burst parameters examined are ν_0 , σ_t , σ_ν , and $dt/d\nu$. In that figure, marker shape indicates the source, while point color represents the duration.

The strongest correlations are those observed with $dt/d\nu$, as shown in the bottom row. The σ_t - σ_ν plot shows little to no correlation, while the σ_t - ν_0 plot shows some evidence of correlation, though with significant statistical scatter in the measurements.

The ν_0 - σ_ν plot appears to exhibit a linear correlation, as was found with previous results obtained over broad frequency ranges but with fewer bursts ([Houde et al. 2019](#); [Chamma et al. 2023](#); [Brown et al. 2024](#)); however, there again remains significant statistical scatter. We fit a line to the complete set and measurements and obtain $\nu_0 = (32.3 \pm 0.1)\sigma_\nu$. Previous values for this correlation are around $\sqrt{8 \ln 2}/0.14 \approx 16.8$, after inverting and scaling from the FWHM for comparison here. Despite the present value being nearly double, we note that, because of the spread in measurements, either fit could be visually attributed to the data.

Two fits are overlaid on the σ_t - ν_0 plot of the form $\sigma_t \propto \nu_0^{-1}$. The blue and orange lines are fit to all bursts with durations longer and shorter than 300 μs , respectively. We find $(1024 \pm 2) \text{ ms}\cdot\text{MHz}$ ν_0^{-1} for the longer FRBs, and $(16.1 \pm 0.1) \text{ ms}\cdot\text{MHz}$ ν_0^{-1} for the ultra-FRBs. Despite the statistical scatter in measurements, the blue line reflects well the trend of measurements, especially the very low frequency bursts from FRB 20180916B. The fit to the ultra-FRBs (orange) also describes the shortest of bursts well. Bursts at around 1.4 GHz, especially from the sources FRB 20200120E and FRB 20220912A, connect the duration gap between the two fits, suggesting a continuum may exist. In that case, the blue and orange fits may represent opposite ends of an envelope. The functional dependence is the prediction of the TRDM and consistent with results reported in [Chamma et al. \(2023\)](#). There is room for other interpretations and

functional forms that may describe this data (such as $\sigma_t \propto \nu_0^{-2}$). However, we focus here on the context that the TRDM provides and follow predictions made by [Kumar et al. \(2024\)](#), which investigates changes to the predictions of the TRDM at short durations and under various propagation effects. In [Kumar et al. \(2024\)](#), bursts that obey the sub-burst slope law and vary in duration by several orders of magnitude can show the sort of separation reflected in the two fits shown.

The blue fit in the $dt/d\nu$ - ν_0 plot, which follows the form $C\nu_0^{-2}$, appears to support the relationship previously reported in [Chamma et al. \(2023\)](#) between these two parameters. Using that earlier fit result, we take $C = -1/(6.1 \times 10^{-5}) \approx 16340 \text{ ms}\cdot\text{MHz}$, inverted for our results here. While caution should be exercised in applying this fit to data from multiple sources, it is evident that the fit qualitatively represents the data reasonably well, including the very low-frequency data from FRB 20180916B. In the inset, the fit passes neatly through the points representing ultra-FRBs, which were not available when C was found. Additionally, we observe significant statistical scatter around 1500 MHz, a characteristic common to data from all the repeating sources included.

Another notable correlation, specifically between $dt/d\nu$ and σ_ν , was also observed in [Chamma et al. \(2023\)](#). We detect this correlation again here and note that, due to measurement noise, the data could potentially be described by relationships of several forms (e.g. $dt/d\nu \propto \sigma_\nu^{-1}$ to σ_ν^{-3}). A conclusive form cannot be inferred from the data. The relationship between $dt/d\nu$ and σ_t is addressed in the previous section, where $dt/d\nu$ is multiplied by frequency to normalize it across datasets.

The interpretation of these relationships within the context of the TRDM, as well as the effect of dispersion and scattering on these relationships, is discussed in Section 5.

4.2 Drift rates

As explained in Section 2, FRBs with multiple components have their drift rates measured by fitting a line through the frequency and time of each component (see the bottom panel of Figure 1 for an example).

After reviewing the measurements and excluding those with relative uncertainties greater than 100% (since even just having the order of magnitude can be informative), a total of 136 drift rates were measured across our burst sample. The magnitudes of the drift rates, $|\Delta t/\Delta \nu|$, span a range of approximately 0.0001 – 6 ms/MHz, covering about five orders of magnitude. Eight of these appear to be plausible positive ‘happy trombones’, which may be due to a physical process or simply a coincidence in the arrival times of otherwise unrelated bursts. In the TRDM, the drift rate sign is determined by the rate of change of the center frequency with the delay time ([Rajabi et al. 2020](#)).

To validate our measurements against the ACF/Gaussian methods, we briefly checked that our drift rates align with previous measurements for bursts that have been studied before. For example, for burst B1 from [Hewitt et al. \(2023\)](#), which contains approximately 40 components with widely varying durations, we measure a drift rate of $-0.14 \pm 0.001 \text{ ms/MHz}$, or $-7.1 \pm 0.1 \text{ MHz/ms}$. The drift rate reported for this burst using a 2D Gaussian fit to the ACF was $-8 \pm 3 \text{ MHz/ms}$, which is consistent within the uncertainties.

Figure 6 shows the drift rate measurements, each multiplied by the mean frequency of their underlying components, plotted against their duration. Overlaid is the fit obtained for the analogous plot of the sub-burst slopes in Figure 4. We observe good agreement between this fit and the drift rate trend, supporting the findings in [Jahns et al.](#)

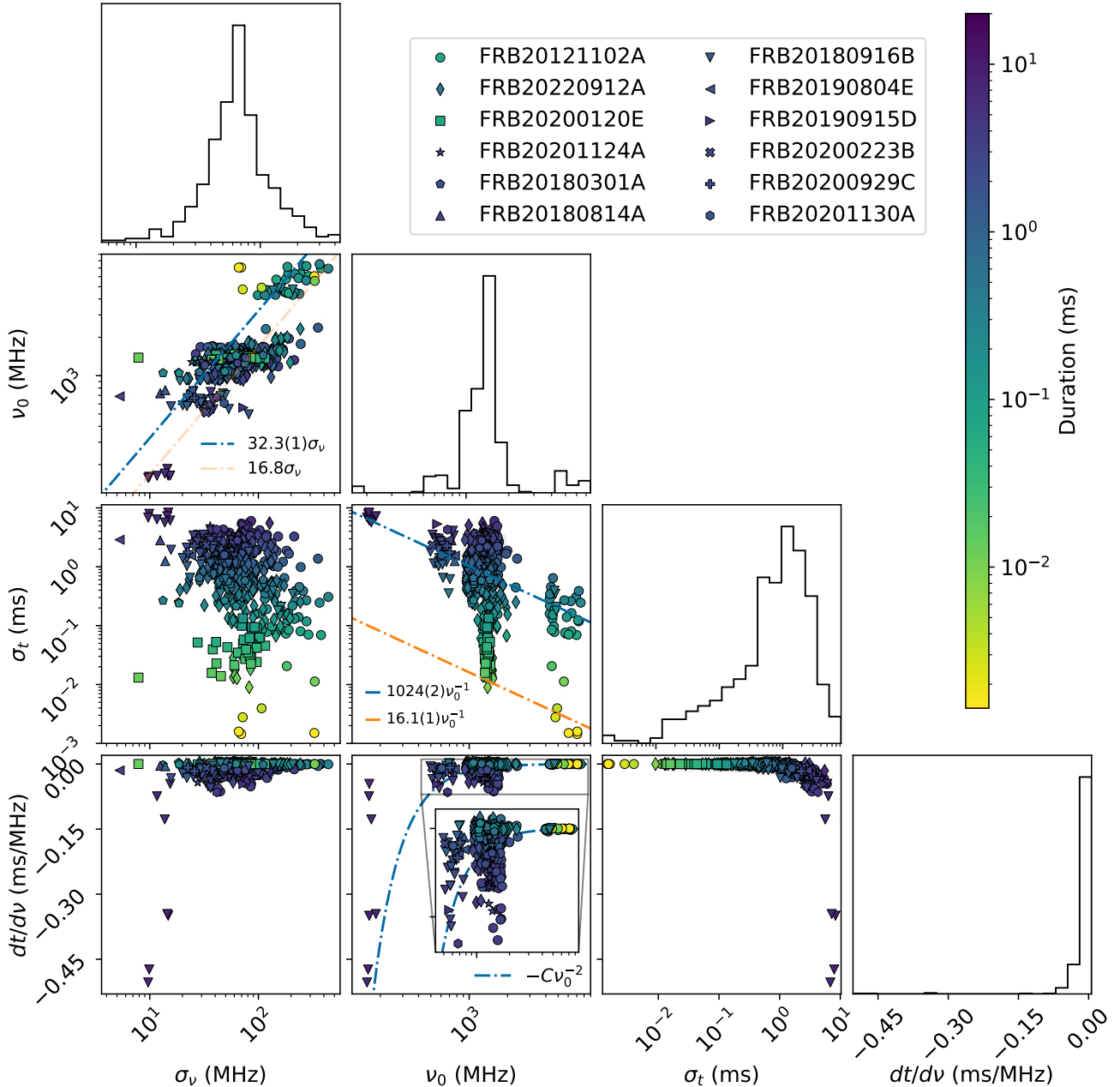


Figure 5. Corner plot of burst properties measured from 12 repeating FRB sources. Marker shape denotes the FRB source. Points are colored by their duration, as indicated by the color bar. Thus the ultra-FRBs can be spotted by their yellow color. The strongest correlations are seen in the three $dt/d\nu$ plots along the bottom row. The blue fit line shown in the $dt/d\nu-\nu_0$ plot is the fit found from FRB 20121102A data reported in [Chamma et al. \(2023\)](#). The blue and orange fit lines in the $\sigma_t-\nu_0$ plot are fit to bursts with duration greater and less than 300 μs . See the text for details.

(2023) and [Brown et al. \(2024\)](#) that these two measurements follow similar trends. Interestingly, the positive drifts approximately follow the negative of this relationship, shown with the faded line, though the small number of points makes it difficult to conclude for certain. This suggests a connection with the negative drifts and the existence of a sign change ([Rajabi et al. 2020](#)), which can explain this aspect of the positive drifts.

The agreement between the sub-burst slope relation and drift rate

measurements can potentially be explained within the context of the TRDM as resulting from minimal or nonexistent variations in the time between a trigger and FRB emission, as discussed in Section 3.1 of [Chamma et al. \(2021\)](#). However, as noted by previous authors, this remains a non-trivial and perhaps unexpected result that warrants deeper study and further validation.

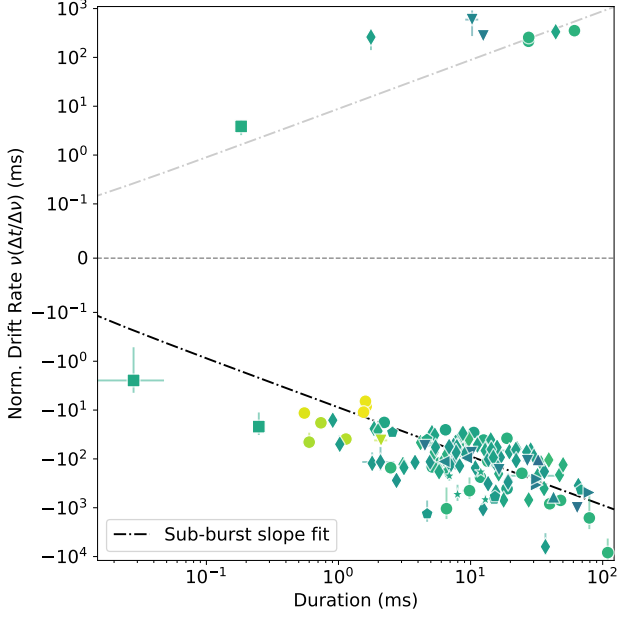


Figure 6. Drift rate measurements of 136 FRBs, normalized by frequency, plotted against duration, are shown analogous to Figure 4, but with a semilog scale on the y-axis. Colors and markers are the same as before. The dashed line represents the corresponding fit found in Figure 4 for the sub-burst slope measurements. Its negative is shown with the faded line. There is good agreement between the drift rates and the relationship found for the sub-burst slopes.

4.3 Method Comparison

In order to assess the differences between the arrival times pipeline and Gaussian methods for spectro-temporal measurements, we selected a subset of bursts and repeated their measurements using each method. We found reasonable agreement between measurement values, with equal or higher precision when using the arrival times pipeline, and significantly higher precision when measuring ultra-FRBs with this method.

The bursts were selected from FRB 20121102A to cover a broad range of durations, and from datasets with sufficiently high time resolution so that the precision in the arrival times pipeline was not limited. The methods applied to each burst were as follows: (a) the arrival times pipeline, (b) fitting a general 2D Gaussian to the ACF of the burst waterfall, followed by computing measurements using the fit parameters (Chamma et al. 2023), (c) directly fitting a general 2D Gaussian, G_{2D} , to the waterfall and computing measurements from the fit parameters, and (d) directly fitting a 2D Gaussian with physically defined parameters including the intra-burst drift, d_t , to the waterfall (eq. 2 of Jahns et al. 2023). In total, 34 bursts were analysed, including two ultra-FRBs from Snelders et al. (2023), nine bursts from Michilli et al. (2018), and 23 bursts from Li et al. (2021). This selection was largely arbitrary, as applying multiple measurement methods to each burst is labor-intensive, requiring thorough review and quality assurance for each measurement. Regardless, this subset was sufficient for our purposes. We initially included 29 bursts from Oostrum et al. (2020) in this multi-method analysis, however, the low time resolution of that dataset affected the precision of the arrival time t_{arr} measured in each channel (see eq. 2), severely limiting the precision of the arrival times method. In such instances, where time

resolution is low, the Gaussian methods generally provide higher precision. Additional bursts were analysed from the datasets listed, but only those yielding quality measurements across all methods were retained. The results of this multi-method comparison are shown in Figures 7 and 8.

Figure 7 displays the measurement values obtained for $dt/d\nu$ across six bursts of roughly increasing durations. As shown, the measurement values from the four applied methods can align closely, as seen for bursts M001 ($\sigma_t = 0.39$ ms) and M01_0136 ($\sigma_t = 2.7$ ms). Across these six bursts, the measurement values are generally of the same order of magnitude, even when applied to ultra-FRBs. However, the largest percent difference between values (i.e. the largest difference in measurements divided by the arrival times measurement) can exceed 1000%. These statements generally apply to the entirety of the subset of bursts analysed. Additionally, the uncertainties for each measurement methods are shown, and we observe that, for longer-duration bursts (the four right-most bursts; remembering $|dt/d\nu| \propto \sigma_t$), uncertainties are small regardless of the method used (though the ACF method does produce very large uncertainties for two of the bursts). This changes significantly for the two ultra-FRBs, B30 and B43, where only the arrival times method yields a relative uncertainty smaller than the measurement value, effectively constraining the sign of the measurement of $dt/d\nu$ (i.e., it does not cross zero). These results therefore support the effectiveness of the arrival times method for ultra-FRBs and demonstrate the limitation of the Gaussian methods.

In Figure 8, the three panels provide additional data highlighting the advantage of the arrival times method. The top panel shows that the arrival times method yields a 16% relative uncertainty for the ultra-FRB B43, whereas the ACF and both direct Gaussian methods result in relative uncertainties exceeding 100%. The middle and bottom panels qualitatively illustrate the relationship between the uncertainty in $dt/d\nu$ and the burst’s duration and $dt/d\nu$ measurement, respectively. Despite fluctuations, we observe that at larger values of duration and sub-burst slope, uncertainties from the arrival times, ACF, and direct Gaussian methods are often comparable (differences arise due to burst waterfall characteristics rather than the method used). Additionally, as the measurement value decreases, the uncertainty from the arrival times method remains relatively constant, while the uncertainty from the ACF and direct Gaussian methods increase by several orders of magnitude.

Although the comparisons presented here are qualitative, they demonstrate the general scenarios that can arise when analysing a diverse array of bursts with varying data resolutions, morphologies, and duration/frequency scales using different methods. Specifically, the arrival times pipeline provides stable precision across several orders of magnitude in duration and sub-burst slope and achieves much higher precision for ultra-FRBs than Gaussian methods without modification, whether fitted to the burst ACF or directly to the waterfall. Nonetheless, there may be strategies that could be explored to improve the precision of Gaussian methods for short durations and steep (vertical) slopes.

There are likely analytical reasons why the Gaussian methods fail at certain duration scales, and we attempted to demonstrate this by deriving the analytical covariance matrix using a computer algebra system (SymPy in this case). However, the computational cost of our initial attempts proved prohibitive. It is straightforward to show that the inverse of derivatives appearing in the covariance matrix (such as $\partial^2 G_{2D} / \partial \sigma_t \partial d_t$) approach infinity at short durations, but without a complete expression, it remains unclear how these terms contribute to the full elements of the covariance matrix that determine the uncertainties.

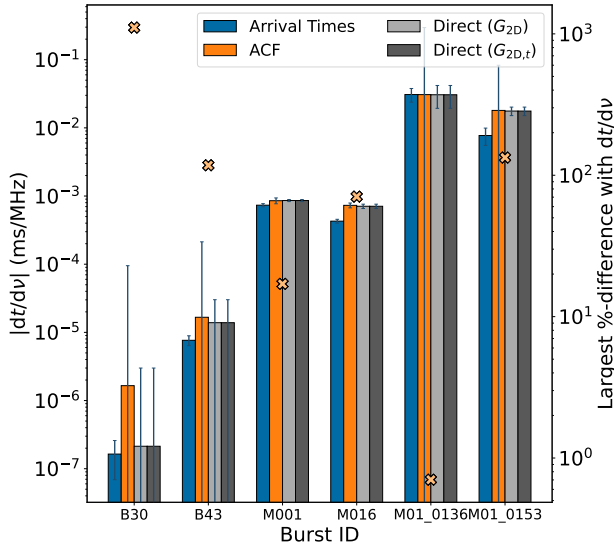


Figure 7. Comparison of measurements of dt/dv for six bursts of roughly increasing duration, repeated using different methods. These methods are the arrival times pipeline (blue), a 2D Gaussian fit to the burst ACF (orange), and a 2D Gaussian fit directly to the burst waterfall (light and dark gray). The light gray represents a generic 2D Gaussian form (see, e.g., Chamma et al. 2023) while the dark gray uses the 2D Gaussian parameterized with physical variables, including the slope introduced by Jahns et al. (2023). Note that these last two result in identical measurements. The peach points show the largest percent difference of the measurement between methods. While measurements are almost identical in some cases, there can also be significant differences between them. The bursts shown are from Snelders et al. (2023) (B30 and B43), Michilli et al. (2018) (M001 and M016), and Li et al. (2021) (M01_0136, M01_0153) and are all from FRB 20121102A.

Nonetheless, we generally recommend using an arrival times oriented approach for ultra-FRBs.

5 DISCUSSION

In this section we discuss the physical interpretation of the spectro-temporal relationships observed in our analysis of burst data using the arrival times pipeline. We examine the effects of interstellar scattering on the observed relationships and on specific burst properties, identifying those most affected by scattering.

A physical interpretation of the sub-burst slope relation observed in Figure 4 is offered by the TRDM of Rajabi et al. (2020). The arrival time t_{arr} , defined and used here as the basis of our measurement method, is equivalent to the delay time t_D , representing the time interval between the (unobserved) trigger and the start of FRB emission. In the TRDM, the predicted relationship between sub-burst slope and duration is scaled by a physical constant such that, using the notation defined earlier,

$$\nu_0 \frac{dt}{dv} = -\left(\frac{\tau'_D}{\tau'_w}\right)\sigma_t, \quad (5)$$

where our earlier fit parameter a is defined by $a \equiv -(\tau'_D/\tau'_w)$, which represents the ratio of the proper delay time to the proper burst duration in the rest frame of the FRB source. Thus, within the context of the TRDM, the scaling of the sub-burst slope–duration relation arises from a constant factor linking the delay time following a trigger

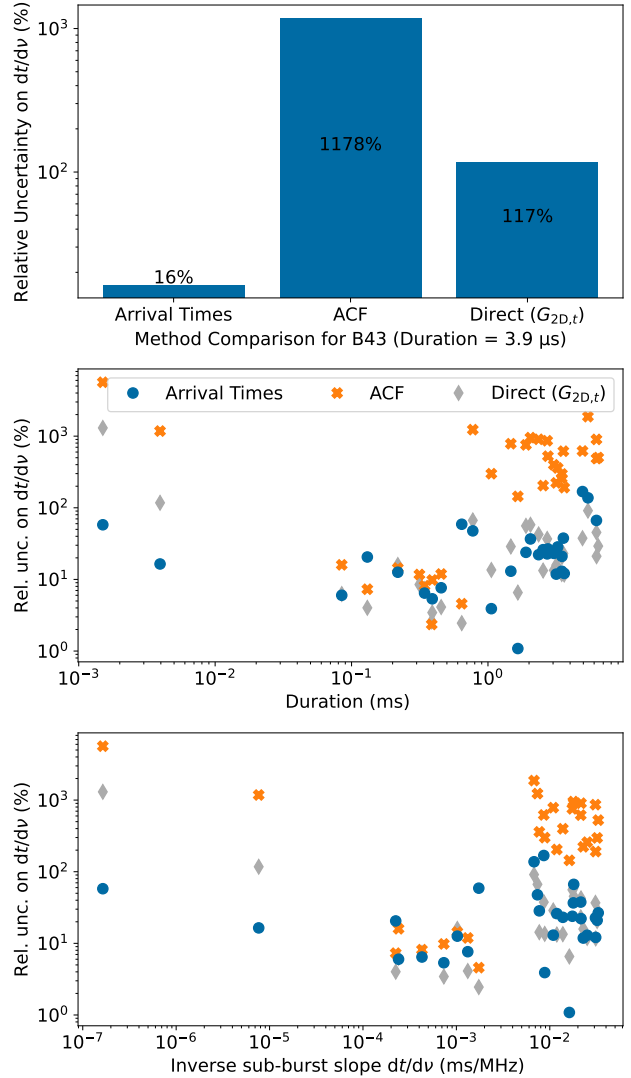


Figure 8. Method comparisons for a subsample of bursts, focusing on the resulting uncertainty following each method. **(top)** Uncertainties between methods focused on the ultra-FRB B43 from Snelders et al. (2023) which has a duration of $3.9 \mu\text{s}$. The uncertainty is prohibitively large when using a Gaussian fit to either the ACF of the burst or directly to the waterfall. **(center)** Uncertainty for a subsample of bursts as a function of burst duration. The circles, x's and diamonds denote the uncertainty when using the arrival times pipeline, ACF, and direct Gaussian methods, respectively. **(bottom)** Same as center panel but as a function of the inverse sub-burst slope. Smaller values of dt/dv indicate a more ‘vertical’ burst. Note that the arrival times uncertainties are either similar to or far below the uncertainties when using other methods, especially with bursts that are short or near vertical.

experienced by an FRB emitter to the resulting duration of an FRB pulse. This model was inspired by the application of Dicke’s superradiance to FRBs (Houde et al. 2019), though it is broadly applicable. It is important to note that beyond the assumption of a fundamentally narrowband emission process, the TRDM is agnostic to the underlying emission mechanism and primarily describes the transformation of the FRB signal by dynamical and relativistic effects.

The slope–frequency relation is a strong correlation that is observed in our results here and predicted in the TRDM (e.g. 7 of

Chamma et al. 2023). Despite three outliers, the addition of low frequency LOFAR data for FRB 20180916B seems to suggest a shared trend between at least that source and FRB 20121102A. This is because the same scaling of the fit shown in the $dt/d\nu-v_0$ panel of Figure 5 describes the FRB 20180916B data and indeed the data from all sources well. In the TRDM the scaling constant for this relationship is equivalent to $1/\tau_D' \nu_e$ where ν_e is the rest frame frequency of emission of the FRB. This relationship is also expected in the context of curvature radiation by charged bunches in the magnetosphere of magnetars (Wang et al. 2022). In this vein, there is growing evidence that favors models of emission with magnetospheric origins, such as a recent scintillation analysis for FRB 20221022A that provided a constraint on the lateral size of the FRB emission region in that source to less than $\sim 3 \times 10^4$ km (Nimmo et al. 2024).

The sub-burst slope relation in the TRDM is derived directly from a more basic relationship between burst duration and frequency, and, with some caveats, there is good evidence of this basic relation in our results. Namely, the TRDM expects $\sigma_T \propto \nu_0^{-1}$ (eqs. 3 and 4 of Rajabi et al. 2020, note the differing definition of ν_0). As discussed in Section 4.1.2, the addition of ultra-FRBs in this analysis makes it clear that while the ultra-FRBs appear to obey this relation, they can form a distinct group on the σ_T-v_0 plot (Kumar et al. 2024). Other forms might also describe this data, given the spread in measurements.

A likely scenario is that the underlying TRDM relations do hold for FRBs but are obfuscated by physical processes, either before, during, or after emission, that add statistical scatter to the observed burst properties. This statistical scatter spans several orders of magnitude for bursts analysed here (such as in the two orders of magnitude spanned by duration measurements for bursts around 1500 MHz) and is an important reason that most burst parameters appear uncorrelated in many narrowband studies. It is therefore important to characterize the extent of this statistical scatter as, assuming the validity of the TRDM's simple assumptions, they may arise directly from the underlying emission mechanism.

An explanation for the behavior of ultra-FRBs in the sub-burst slope law (Figure 4) and σ_T-v_0 relation is put forward by Kumar et al. (2024). They show through simulation that the effects of interstellar scattering and residual dispersion modifies the sub-burst slope law in a way that affects ultra-FRBs differently from longer duration FRBs. This includes the presence of a positive sub-burst slope 'bump' for ultra-FRBs, which we can observe in our results.

Interstellar scattering can significantly affect the durations of measured bursts and, in principle, delay the arrival times of pulses in a frequency-dependent manner, thereby impacting the measurement of the sub-burst slope. The extent of this effect depends on the scattering timescale, which quantifies the amount of scattering present. For sources with significant scattering, deviations from the ideal sub-burst slope law can be substantial, particularly at low frequencies and for longer-duration bursts (Kumar et al. 2024). At lower scattering timescales, these deviations become less pronounced. Since the ultra-FRBs used here were at a higher frequency, the effects on this study are likely also less pronounced.

One natural extension of the arrival times method is measuring and quantifying interstellar scattering on FRBs. This can be done by replacing the Gaussian profile fit to each frequency channel of an FRB waterfall (eq. 1) with a profile shape that consists of a Gaussian convolved with a scattering tail.

This can serve as a more accurate model for FRBs that are less Gaussian-like in their pulse shape while also providing an optimized measurement of the scattering timescale as a function of frequency.

Further adjustments would be necessary to integrate this change into the pipeline, such as updating the definition of duration used,

and some care is needed to see how the pipeline behaves for both bursts that exhibit scattering and those that do not. We leave this analysis to future research efforts. We also note that while bursts with potential scattering tails were observed in our sample, they were the vast minority and the majority were well described by a Gaussian profile.

Evidently, there are rich connections between observed spectro-temporal relationships and the physical models surrounding FRBs. We therefore believe that continued and deep monitoring of repeating FRB sources with the intent of matching the diversity of bursts available for FRB 20121102A would be invaluable to this type of spectro-temporal analysis and provide significant insights and constraints on FRB emission mechanisms.

6 SUMMARY AND CONCLUSIONS

We have developed and applied a measurement pipeline based on using the arrival times of an FRB pulse in each frequency channel of its dynamic spectrum to perform sub-burst slope/intra-burst drift measurements. This was done in order to obtain precise spectro-temporal measurements of recently observed ultra-FRBs; FRBs with durations on the order of microseconds or less. The pipeline successfully provided high precision measurements of the slope especially in ultra-FRBs, whereas earlier 2D Gaussian techniques yield measurements with uncertainties often much larger than the measurement value. Drift rates were also measured for bursts with multiple components, yielding a total of 136 measurements.

The arrival times pipeline was successfully applied to a total of 503 FRBs from 12 repeating sources. The focus of our analysis was on the repeating sources FRB 20121102A, FRB 20220912A, and FRB 20200120E, all of which have recently exhibited ultra-FRBs. Bursts from FRB 20121102A spanned the broadest duration and frequency range in our sample, largely due to the many years of observation that source has enjoyed. These bursts along with the remaining data span 110 MHz up to 8 GHz in frequency and 1.4 μ s up to 6 ms in duration, and therefore constitute a sample of bursts that cover several orders of magnitude of burst properties as well as morphologies. Sub-burst slope $dt/d\nu$, center frequency ν_0 , bandwidth σ_ν , and duration σ_T measurements were obtained for each of these bursts using the arrival times pipeline.

Analysing the spectro-temporal relationships between these properties showed once again the known strong correlation between sub-burst slope and duration, the scaling of which was consistent with that found in earlier studies using the 2D Gaussian techniques. For the bursts from FRB 20121102A, we found $\nu(dt/d\nu) \simeq (-8.9 \pm 0.1)\sigma_T$. Other strong correlations were observed between the $dt/d\nu-\sigma_\nu$ and $dt/d\nu-v_0$ relations, this last one showing a single scaling describing the data from all sources well. The addition of ultra-FRBs showed a correlation between σ_T and ν_0 , though appear distinct from longer duration FRBs. For the remaining $\sigma_T-\sigma_\nu$ and $\nu_0-\sigma_\nu$ relations, there was significant statistical scatter between the measurements. An example of this statistical scatter is the nearly 4 orders of magnitude spanned by duration measurements for bursts observed at ~ 1500 MHz. The drift rates measured showed good agreement with the analogous relation between sub-burst slope and duration and seem to extend the trend laid by the sub-burst slopes.

Comparing measurements obtained from the arrival times pipeline with multiple 2D Gaussian techniques, including fitting to the burst ACF and fitting directly to the burst waterfall, generally revealed agreement between the methods with certain factors to keep in mind that could lead to significant differences. The first being that the Gaus-

sian methods yield prohibitively large relative uncertainties on dt/dv measurements when applied to ultra-FRBs, while the arrival times pipeline yields the same measurements with relative uncertainties on the order of a few percent. At longer durations the methods can agree almost precisely, with differences attributable to complicated burst morphologies or RFI. In that regard, measurements from the arrival times pipeline can be quite sensitive to RFI or a bad channel, where a few misplaced arrival times can skew a measurement. The arrival times pipeline can also be severely limited and give higher relative uncertainties than Gaussian methods if the time resolution of the data is insufficiently high. With these factors in mind, however, the arrival times pipeline offers equal or higher precision than Gaussian methods at all FRB duration scales observed with this burst sample.

A simple linear model was applied when obtaining measurements of the sub-burst slope dt/dv in this study, however the arrival times method offers straightforward extensions that can accommodate more complicated drifting morphologies.

While interstellar scattering and the DM of a source remain significant and often dominating factors in the accuracy (or inaccuracy) of spectro-temporal measurements, the arrival times pipeline offers an adaptable and firm foundation for obtaining numerically precise spectro-temporal measurements from FRBs. The arrival times method is available in an online package with documentation and open to contributions from the community.

ACKNOWLEDGEMENTS

The authors would like to thank Sofia Sheikh, Wael Farah, Danté Hewitt, Mark Snelders, and Yong-Kun Zhang for their help in accessing their respective datasets and for additional assistance in reading it. We are also grateful to Martin Houde for their extensive feedback and discussions of the text.

F.R.'s research is supported by the Natural Sciences and Engineering Research Council of Canada (NSERC) Discovery Grant RGPIN-2024-06346.

DATA AVAILABILITY

All measurements and scripts produced during the analysis are available online at <https://zenodo.org/records/13357030>.

The arrival times pipeline is packaged with FRBGUI, available at <https://github.com/mef51/frbgui>. Technical documentation and tutorials on using the arrival times pipeline is available at <https://frbgui.readthedocs.io/arrivaltimes>.

REFERENCES

- Aggarwal K., Agarwal D., Lewis E. F., Anna-Thomas R., Tremblay J. C., Burke-Spolaor S., McLaughlin M. A., Lorimer D. R., 2021, *The Astrophysical Journal*, 922, 115
- Bassa C. G., et al., 2017, *The Astrophysical Journal*, 843, L8
- Bhardwaj M., et al., 2021, *The Astrophysical Journal Letters*, 910, L18
- Boggs P. T., Rogers J. E., 1990, *Contemporary mathematics*, 112, 183
- Brown K., Chamma M. A., Rajabi F., Kumar A., Rajabi H., Houde M., 2024, *Monthly Notices of the Royal Astronomical Society: Letters*, 529, L152
- CHIME/FRB 2019, *Nature*, 566, 230
- CHIME/FRB 2020, *Nature*, 582, 351
- CHIME/FRB et al., 2021, *ApJS*, 257, 59
- CHIME/FRB et al., 2023, *ApJ*, 947, 83
- Chamma M. A., Rajabi F., Wyenberg C. M., Mathews A., Houde M., 2021, *Monthly Notices of the Royal Astronomical Society*, 507, 246
- Chamma M. A., Rajabi F., Kumar A., Houde M., 2023, *MNRAS*, 522, 3036
- Chatterjee S., et al., 2017, *Nature*, 541, 58
- Cruces M., et al., 2020, *Monthly Notices of the Royal Astronomical Society*, 500, 448
- Faber J. T., et al., 2023, doi:10.48550/arxiv.2312.14133
- Fonseca E., et al., 2023, doi:10.48550/arXiv.2311.05829
- Gajjar V., et al., 2018, *The Astrophysical Journal*, 863, 2
- Hessels J. W. T., et al., 2019, *The Astrophysical Journal*, 876, L23
- Hewitt D. M., et al., 2022, *MNRAS*, 515, 3577
- Hewitt D. M., et al., 2023, *MNRAS*, 526, 2039
- Hewitt D. M., et al., 2024, *Monthly Notices of the Royal Astronomical Society*
- Hilmarsson G. H., Spitler L. G., Main R. A., Li D. Z., 2021, *Monthly Notices of the Royal Astronomical Society*, 508, 5354
- Houde M., Rajabi F., Gaensler B. M., Mathews A., Tranchant V., 2019, *Monthly Notices of the Royal Astronomical Society*, 482, 5492
- Jahns J. N., et al., 2023, *MNRAS*, 519, 666
- Kirsten F., et al., 2022, *Nature*, 602, 585
- Kumar A., Rajabi F., Houde M., 2024, arXiv:2412.00232
- Li D., et al., 2021, *Nature*, 598, 267
- Luo R., et al., 2020, *Nature*, 586, 693
- Marcote B., et al., 2017, *ApJ*, 834, L8
- Marthi V. R., Gautam T., Li D. Z., Lin H.-H., Main R. A., Naidu A., Pen U.-L., Wharton R. S., 2020, *Monthly Notices of the Royal Astronomical Society: Letters*, 499, L16
- Michilli D., et al., 2018, *Nature*, 553, 182
- Nimmo K., et al., 2022, *Nature Astronomy*, 6, 393
- Nimmo K., et al., 2023, *MNRAS*, 520, 2281
- Nimmo K., et al., 2024, doi:10.48550/ARXIV.2406.11053
- Oostrum L. C., et al., 2020, *Astronomy & Astrophysics*, 635, A61
- Pastor-Marazuela I., et al., 2021, *Nature*, 596, 505
- Pearlman A. B., et al., 2023, doi:10.48550/arXiv.2308.10930
- Petroff E., Hessels J. W. T., Lorimer D. R., 2022, *The Astronomy and Astrophysics Review*, 30
- Pleunis Z., et al., 2021a, *The Astrophysical Journal Letters*, 911, L3
- Pleunis Z., et al., 2021b, *The Astrophysical Journal*, 923, 1
- Rajabi F., Chamma M. A., Wyenberg C. M., Mathews A., Houde M., 2020, *Monthly Notices of the Royal Astronomical Society*, 498, 4936
- Ravi V., et al., 2023, *The Astrophysical Journal Letters*, 949, L3
- Scholz P., et al., 2016, *ApJ*, 833, 177
- Sheikh S. Z., et al., 2024a, *MNRAS*, 527, 10425
- Sheikh S. Z., et al., 2024b, *Monthly Notices of the Royal Astronomical Society*, 534, 1949
- Snelders M. P., et al., 2023, *Nature Astronomy*
- Spitler L. G., et al., 2016, *Nature*, 531, 202
- Tendulkar S. P., et al., 2017, *ApJ*, 834, L7
- Tendulkar S. P., et al., 2021, *The Astrophysical Journal Letters*, 908, L12
- Wang W.-Y., Yang Y.-P., Niu C.-H., Xu R., Zhang B., 2022, *The Astrophysical Journal*, 927, 105
- Zhang Y.-K., et al., 2023, *The Astrophysical Journal*, 955, 142

APPENDIX A: TABLE OF ULTRA-FRB MEASUREMENTS

Abridged table of measurements obtained for a subset of ultra-FRBs. The full table with measurements of all bursts and additional columns is available at <https://zenodo.org/records/13357030>.

APPENDIX B: MEASURING MICROSLOT FORESTS WITH THE ARRIVAL TIMES PIPELINE

Though challenging, the arrival times pipeline can be used to obtain measurements for the components of bursts that exhibit dense microslot forests with dozens of components, such as those analysed in this study from Hewitt et al. (2023) and Zhang et al. (2023). We briefly describe here our approach to obtaining measurements from these waterfalls as an example of applying the arrival times pipeline

Source	Burst ID	DM pc/cm ³	ν_0 MHz	σ_t μ s	σ_ν MHz	dt/d ν ms/MHz
FRB 20121102A	burst-B06-a	560.105	7075 \pm 10	1.44 \pm 0.1	69 \pm 10	(-1.2 \pm 0.3) \times 10 ⁻⁵
	burst-B30	560.105	6048 \pm 25	1.50 \pm 0.1	327 \pm 26	(1.6 \pm 0.9) \times 10 ⁻⁷
	burst-B06-b	560.105	7073 \pm 11	1.59 \pm 0.2	66 \pm 11	(-3.3 \pm 1.7) \times 10 ⁻⁵
	burst-B07	560.105	4760 \pm 14	2.78 \pm 0.3	72 \pm 15	(9.5 \pm 4.6) \times 10 ⁻⁶
	burst-B43	560.105	4915 \pm 9	3.95 \pm 0.1	107 \pm 9	(-7.7 \pm 1.3) \times 10 ⁻⁶
	burst-B38	560.105	5551 \pm 52	11.24 \pm 1.5	330 \pm 56	(-2.9 \pm 0.9) \times 10 ⁻⁵
	M006	560.105	4459 \pm 11	20.55 \pm 1.3	183 \pm 12	(2.9 \pm 0.3) \times 10 ⁻⁵
	11A-b	560.105	6984 \pm 30	69.33 \pm 6.1	377 \pm 32	(-6.7 \pm 2.3) \times 10 ⁻⁵
	11Q	560.105	6054 \pm 16	70.46 \pm 2.9	289 \pm 16	(-1.8 \pm 0.1) \times 10 ⁻⁴
	11G	560.105	5751 \pm 27	73.26 \pm 17.2	180 \pm 27	(-2.0 \pm 1.0) \times 10 ⁻⁴
	11N	560.105	5685 \pm 12	76.12 \pm 8.7	146 \pm 12	(-2.8 \pm 0.4) \times 10 ⁻⁴
	M013-b	560.105	4680 \pm 13	78.22 \pm 2.8	120 \pm 14	(-2.3 \pm 0.3) \times 10 ⁻⁴
	11A-c	560.105	6340 \pm 18	80.17 \pm 10.7	244 \pm 18	(-9.0 \pm 2.2) \times 10 ⁻⁵
	M014	560.105	4458 \pm 13	84.75 \pm 1.3	190 \pm 14	(-2.4 \pm 0.1) \times 10 ⁻⁴
	M013-c	560.105	4632 \pm 13	97.04 \pm 6.3	133 \pm 14	(-2.6 \pm 0.7) \times 10 ⁻⁴
	11H	560.105	7262 \pm 11	118.33 \pm 2.4	277 \pm 11	(-2.3 \pm 0.1) \times 10 ⁻⁴
12B-a	560.105	7164 \pm 11	123.74 \pm 6.7	185 \pm 12	(-2.8 \pm 2.3) \times 10 ⁻⁴	
...
FRB 20220912A	B2-j	219.375	1396 \pm 5	8.97 \pm 0.1	82 \pm 5	(4.2 \pm 2.0) \times 10 ⁻⁶
	B1-s	219.356	1542 \pm 5	12.69 \pm 4.5	63 \pm 5	(2.9 \pm 2.1) \times 10 ⁻⁵
	B1-h	219.356	1534 \pm 4	13.17 \pm 3.9	59 \pm 4	(4.3 \pm 1.3) \times 10 ⁻⁵
	B1-p	219.356	1519 \pm 5	14.50 \pm 1.3	61 \pm 5	(-6.2 \pm 4.1) \times 10 ⁻⁶
	B1-k	219.356	1530 \pm 4	17.36 \pm 7.6	60 \pm 4	(-3.1 \pm 1.8) \times 10 ⁻⁴
	B1-o	219.356	1521 \pm 5	17.83 \pm 4.0	61 \pm 5	(-3.1 \pm 1.1) \times 10 ⁻⁵
	B2-i	219.375	1436 \pm 6	18.08 \pm 0.6	85 \pm 6	(9.7 \pm 2.0) \times 10 ⁻⁶
	B1-i	219.356	1533 \pm 5	28.25 \pm 1.9	58 \pm 5	(8.5 \pm 7.4) \times 10 ⁻⁶
	B1-l	219.356	1527 \pm 4	46.01 \pm 45.5	61 \pm 4	(-3.5 \pm 0.7) \times 10 ⁻⁴
	B2-f	219.375	1461 \pm 6	53.18 \pm 46.0	91 \pm 6	(-1.5 \pm 1.1) \times 10 ⁻⁴
	9-06-g	219.356	1227 \pm 3	60.48 \pm 2.7	106 \pm 3	(2.6 \pm 0.5) \times 10 ⁻⁵
	B24-a	219.356	1968 \pm 5	67.36 \pm 5.7	145 \pm 5	(-3.3 \pm 1.7) \times 10 ⁻⁵
	9-06-c	219.356	1255 \pm 3	83.73 \pm 5.5	110 \pm 3	(-1.7 \pm 0.1) \times 10 ⁻⁴
	B01-b	219.356	1650 \pm 23	92.09 \pm 9.3	163 \pm 20	(-1.5 \pm 0.3) \times 10 ⁻⁴
	B12-d	219.356	1661 \pm 9	98.36 \pm 2.3	159 \pm 9	(-1.3 \pm 0.2) \times 10 ⁻⁴
	9-06-f	219.356	1232 \pm 3	105.73 \pm 3.8	107 \pm 3	(-1.1 \pm 0.1) \times 10 ⁻⁴
...
FRB 20200120E	20220223-B1	87.7527	1385 \pm 0	13.10 \pm 0.7	8 \pm 0	(2.4 \pm 2.1) \times 10 ⁻⁵
	B3-a	87.75	1346 \pm 4	13.86 \pm 2.6	45 \pm 4	(-3.9 \pm 0.8) \times 10 ⁻⁵
	B3-b	87.75	1331 \pm 4	15.78 \pm 9.0	37 \pm 4	(3.6 \pm 1.4) \times 10 ⁻⁵
	20220114-B41	87.7527	1469 \pm 12	21.25 \pm 4.4	60 \pm 13	(-1.7 \pm 1.2) \times 10 ⁻⁴
	20220114-B51	87.7527	1377 \pm 13	22.49 \pm 4.8	85 \pm 14	(-2.5 \pm 0.7) \times 10 ⁻⁴
	B2-a	87.75	1344 \pm 5	22.75 \pm 0.7	41 \pm 5	(-4.4 \pm 1.3) \times 10 ⁻⁵
	20220114-B19	87.7527	1387 \pm 15	24.08 \pm 3.0	96 \pm 16	(1.1 \pm 0.9) \times 10 ⁻⁴
	20220114-B47	87.7527	1326 \pm 7	27.13 \pm 1.5	76 \pm 8	(4.8 \pm 1.8) \times 10 ⁻⁵
	20220114-B37	87.7527	1423 \pm 8	28.59 \pm 1.4	85 \pm 8	(7.6 \pm 2.4) \times 10 ⁻⁵
	20220114-B49	87.7527	1398 \pm 11	29.59 \pm 2.1	83 \pm 11	(8.5 \pm 3.4) \times 10 ⁻⁵
	20220114-B32	87.7527	1402 \pm 15	32.05 \pm 5.0	83 \pm 15	(-1.6 \pm 1.2) \times 10 ⁻⁴
	20220114-B34	87.7527	1442 \pm 7	32.18 \pm 2.5	73 \pm 8	(-1.8 \pm 0.6) \times 10 ⁻⁴
	20220114-B42	87.7527	1409 \pm 12	34.81 \pm 4.8	65 \pm 12	(-1.2 \pm 1.1) \times 10 ⁻⁴
	20220114-B18-b	87.7527	1361 \pm 12	34.83 \pm 4.2	82 \pm 13	(-2.2 \pm 1.7) \times 10 ⁻⁴
	20220114-B50	87.7527	1421 \pm 16	34.88 \pm 2.3	80 \pm 16	(1.1 \pm 0.6) \times 10 ⁻⁴
	20220221-B1	87.7527	1374 \pm 12	39.31 \pm 4.1	77 \pm 12	(-1.7 \pm 0.9) \times 10 ⁻⁴
	20220114-B40	87.7527	1318 \pm 4	39.52 \pm 5.0	38 \pm 4	(-1.5 \pm 0.7) \times 10 ⁻⁴
	20220114-B48	87.7527	1365 \pm 17	42.14 \pm 4.9	96 \pm 18	(2.6 \pm 2.2) \times 10 ⁻⁴
	20220114-B13-b	87.7527	1358 \pm 14	42.32 \pm 3.1	94 \pm 15	(-1.4 \pm 0.5) \times 10 ⁻⁴
	B4	87.75	1378 \pm 5	43.06 \pm 1.1	52 \pm 5	(-1.6 \pm 0.3) \times 10 ⁻⁴
	20220114-B23	87.7527	1374 \pm 16	43.72 \pm 5.3	93 \pm 17	(-3.6 \pm 0.7) \times 10 ⁻⁴
	20220114-B13-a	87.7527	1363 \pm 24	45.67 \pm 5.5	115 \pm 27	(2.8 \pm 1.2) \times 10 ⁻⁴
	20220114-B22	87.7527	1390 \pm 17	47.57 \pm 7.6	88 \pm 18	(-2.8 \pm 2.0) \times 10 ⁻⁴
	20220114-B21	87.7527	1415 \pm 13	49.56 \pm 3.4	72 \pm 13	(-1.0 \pm 0.4) \times 10 ⁻⁴
20220114-B26	87.7527	1358 \pm 12	51.36 \pm 3.8	84 \pm 13	(-4.1 \pm 1.1) \times 10 ⁻⁴	
...

Table A1. Abridged table of spectro-temporal measurements obtained for a subset of ultra-FRBs using the arrival times method. Rows are organized by source and sorted by the sub-burst duration σ_t in ascending order. The full table with measurements of all 503 bursts and additional columns is available online at <https://zenodo.org/records/13357030>.

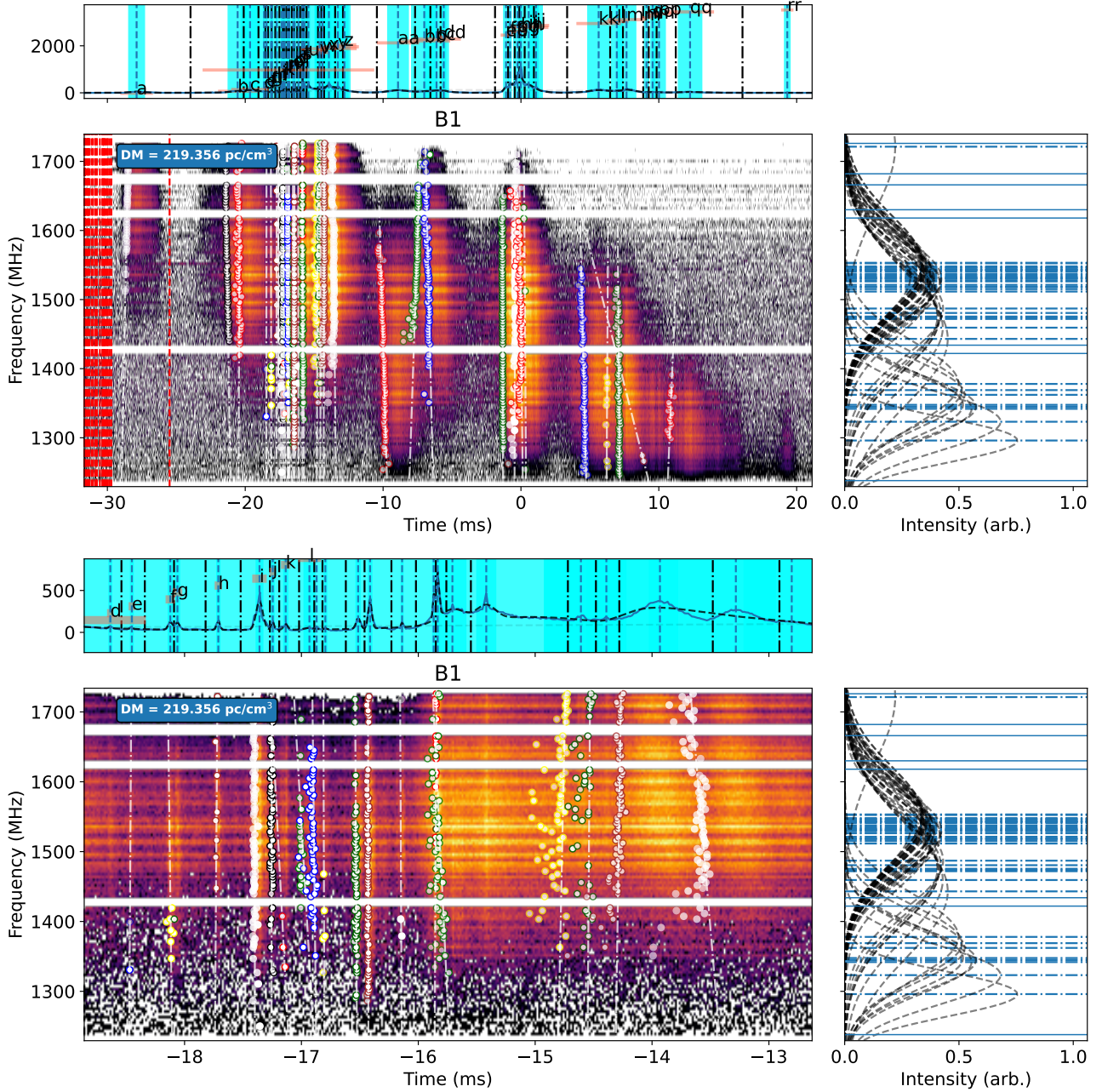


Figure B1. Results of analysing microshot forest burst B1 of Hewitt et al. (2023) with the arrival times pipeline using a manual lists of burst positions (blue dashed lines) and widths as initial guesses and manual cuts (black dash-dot lines) to separate components. Top waterfall shows the full B1 burst, while the bottom shows a zoomed in view of a very active few milliseconds starting at around -18 ms with many sub-millisecond pulses. This bottom panel demonstrates well the challenges of analysing microshots; we see several pulses are well measured, several more have inaccurate sub-burst slope measurements, and a few still are missed completely due to their blended state, short duration, and/or faintness.

to such bursts. We also describe the challenges and issues faced, and how many components could not be usefully measured due to significant blending.

As explained in Section 2, an early step of the arrival times pipeline is to find a fit to the one dimensional integrated time series of the waterfall. For burst B1 of Hewitt et al. (2023), we note 44 components can be distinguished visually from the time series, which poses a significant computational challenge to the fitting algorithm. Thus it is important as much as possible to provide a strong initial guess

to the algorithm for there to be an accurate solution found in a reasonable amount of time. In the arrival times pipeline, this means providing a long list of t_0 s specifying the precise time of each of the 44 burst components. Additionally, we specified a corresponding list of pulse durations σ_t s that was necessary for a reasonably accurate solution. Because of the prevalent presence of blending, we also carefully chose the locations of manual cuts between components as best as possible to indicate what data should be cutout when finding fits in each frequency channel. Despite the success of this

in several components, if two components are significantly blended together then the manual cut, other than being difficult to place, is also insufficient in overcoming the fact that the data of the two blended components obscure one another. With a good initial guess it takes about 20 minutes of computation on an M2 chip on a laptop to perform the measurements of burst B1's components.

The result of applying this process yields many usable measurements but also many unusable measurements, either because of large uncertainties caused by blending or the difficulty of visually confirming the measurement of a faint or blended component. For example, for burst B1 [Hewitt et al. \(2023\)](#), of the 44 components identified manually, only about 20 are used, and the rest are excluded due to relative uncertainties on their duration greater than 100%, relative uncertainties on their sub-burst slope greater than 100%, an insufficient number of well fit channels to obtain a complete measurement, or a combination of all three issues.

Figure B1 shows results from the arrival times pipeline for burst B1 that displays the range of success found in measuring the microshots. Many components are well-measured, while many are missed or yield inaccurate measurements with large uncertainties.

APPENDIX C: DM OPTIMIZATION USING THE SUB-BURST SLOPE RELATION

Assuming the sub-burst slope relation applies to all FRBs, it can be used to define an optimal or corrected DM that is associated with the repeating FRB source. We summarize here strategies from the literature that have been used so far to do so and describe our own efforts with the measurements presented here.

Given a set of measurements of spectro-temporal properties from FRBs one must decide what DM at which to display them. A simple choice is to simply display the measurements at each burst's individually determined DM. This is a valid choice and can be sufficient. However, given the expected relationship between the sub-burst slope and duration, we can apply a single DM to a cohort of bursts (preferably bursts that were emitted close in time to account for long-term changes in the DM) and impose the assumption that bursts that deviate from the sub-burst slope relation are over- or under- dispersed. Because the measurements of $dt/d\nu$ are affected by the DM applied, this implies the existence of an optimal DM where this assumption holds best. We may interpret this optimal DM as the 'real' DM, absent of contributions to the DM that arise from propagation away from the source. That is, assuming the veracity of the sub-burst slope relation, it can be used to correct the DM observed and precisely associate a DM to the source environment.

One way of finding this optimal DM is to repeat measurements on a grid of DMs and choose the DM that minimizes deviations from the sub-burst slope relation, as was done in [Chamma et al. \(2021\)](#), [Chamma et al. \(2023\)](#), and [Brown et al. \(2024\)](#). The main disadvantage of this approach is the time-consuming nature of repeating measurements over many DMs.

A more direct quantitative approach was developed and applied by [Jahns et al. \(2023\)](#) for bursts from FRB 20121102A, by assuming that small burst-to-burst fluctuations in DM are due to drifting behaviour (as opposed to changes in ion column density) and that the sub-burst slope relation extends to very sharp short duration bursts. As our results for ultra-FRBs strongly bear this last assumption out (Figure 4), we will apply this scheme to the measurements presented here.

Following [Jahns et al. \(2023\)](#), a fit of the form $dt/d\nu \equiv d_t(\sigma_t) = -b\sigma_t + c$ is found for the group of burst measurements from a source that have been obtained at the same DM (DM_{applied}). Note that

these fits are similar to the form of fits tabulated in Table 2, except without the multiplication by the frequency ν . Then, interpreting the fit parameter c as 'residual' intra-burst drift, the resulting deviation from the real DM, δDM , is calculated according to

$$\delta DM = -\frac{1}{2} \frac{\nu^3}{a_{DM}} d_t, \quad (C1)$$

where a_{DM} is the dispersion constant, c is substituted for d_t , and we take ν as the mean burst frequency for the dataset considered. Note that this δDM can also be found on a burst by burst basis, but this analysis is not considered here. In this scheme, we expect b to remain roughly the same since it corresponds (up to a factor of ν) to the a parameter in the sub-burst slope relation, and we expect c to get smaller as the data gets closer to the 'real' DM. The 'real' DM is then found through

$$DM_{\text{real}} = DM_{\text{applied}} + \delta DM. \quad (C2)$$

We will repeat this process iteratively, and the obtained DM_{real} is used as the applied DM in the following stage.

We apply this process for the sources FRB 20121102A and FRB 20220912A separately. Note that we exclude the many bursts from [Hewitt et al. \(2022\)](#) for FRB 20121102A due to their different applied starting DM and burst B1 from [Hewitt et al. \(2023\)](#) for FRB 20220912A due to the presence of significant blending. The starting DM used is the DM of the shortest (or nearly the shortest) burst from that source. In the case of FRB 20121102A that burst is the microburst B30 of [Snelders et al. \(2023\)](#), and burst B1 of [Hewitt et al. \(2023\)](#) for FRB 20220912A. The results of this are shown in Table C1.

In general we see that the value of c increases after each round. We also note that the scatter of points increases slightly with each round (not shown). Both behaviours are contrary to expectations and may indicate a divergent solution. The value of b for each dataset is consistent with the sub-burst slope relation fits (Table 2) once scaled by the mean frequency for that dataset. The value of DM_{real} decreases in each round from the initial DM. A possible interpretation of these results is that the initial DM applied is sufficiently optimized that this process does not give much improvement, though for FRB 20121102A our DM value of 560.105 pc/cm^3 is different from the value obtained in [Jahns et al. \(2023\)](#), which was 562.41 pc/cm^3 . We cannot conclude this without first applying this process from a different starting DM, which is beyond the scope of this paper.

Despite the time consuming efforts of repeating and confirming measurements at different DMs, using the sub-burst slope relation with hundreds or thousands of bursts on a short timescale to associate a precise DM to a source is potentially an important technique for probing the source environment of a repeating FRB.

This paper has been typeset from a $\text{\TeX}/\text{\LaTeX}$ file prepared by the author.

FRB 20121102A					
Step	DM_{app}	b (MHz⁻¹)	c (ms/MHz)	δDM	DM_{real}
1.	560.105	-4.1×10^{-3}	8×10^{-6}	-0.0119	560.093
2.	560.093	-4.56×10^{-3}	9.6×10^{-6}	-0.016	560.077
3.	560.077	-4.7×10^{-3}	1.1×10^{-5}	-0.017	560.060
FRB 20220912A					
1.	219.356	-7.09×10^{-3}	1.04×10^{-3}	-0.208	219.148
2.	219.148	-8.2×10^{-3}	2.5×10^{-3}	-0.488	218.659

Table C1. DM Bootstrapping for FRB 20121102A and FRB 20220912A. Note that we exclude the microshot bursts for FRB 20220912A from [Hewitt et al. \(2023\)](#) due to significant blending. Units of DM are pc/cm³.